Extension of the Particle X-ray Coincidence Technique (PXCT) to Discrete Resonances and Astrophysical Reaction Rates

L. J. Sun[1],[*] J. Dopfer[1,2], A. Adams[1,2], C. Wrede[1,2],[†] A. Banerjee[3], B. A. Brown[1,2],
R. Mahajan[1], T. Rauscher[4,5], C. Sumithrarachchi[1], D. Weisshaar[1], and T. Wheeler[1,2,6]
[1]*Facility for Rare Isotope Beams, Michigan State University, East Lansing, Michigan 48824, USA*
[2]*Department of Physics and Astronomy, Michigan State University, East Lansing, Michigan 48824, USA*
[3]*Saha Institute of Nuclear Physics, Kolkata, West Bengal 700064, India*
[4]*Department of Physics, University of Basel, 4056 Basel, Switzerland*
[5]*Centre for Astrophysics Research, University of Hertfordshire, Hatfield AL10 9AB, UK*
[6]*Department of Computational Mathematics, Science, and Engineering,*
Michigan State University, East Lansing, Michigan 48824, USA

(Dated: June 12, 2024)

The strength of the NiCu cycle is predicted to significantly impact the modeling of Type I X-ray burst light curves and the composition of the burst ashes. Addressing the competition between the ^{59}Cu$(p,\gamma)^{60}$Zn and ^{59}Cu$(p,\alpha)^{56}$Ni reactions at stellar temperatures requires accurate nuclear physics inputs, such as the lifetimes of ^{60}Zn resonances. The Particle X-ray Coincidence Technique (PXCT) was originally developed to measure average lifetimes in the 10^{-17}–10^{-15} s range for proton-unbound states populated by electron capture (EC). We have designed and built a detection system at the Facility for Rare Isotope Beams (FRIB) that extends PXCT to measure the lifetimes and decay branching ratios of discrete resonances populated by EC/β^+ decay. Detailed theoretical calculations, Monte Carlo simulations, and performance tests using radioactive sources have been conducted to demonstrate the feasibility of employing the PXCT system for its first planned experiment in the stopped-beam area of FRIB. Our goal is to obtain essential nuclear data from ^{60}Ga EC/β^+ decay to constrain the ^{59}Cu$(p,\gamma)^{60}$Zn and ^{59}Cu$(p,\alpha)^{56}$Ni thermonuclear reaction rates, which will contribute to a more comprehensive understanding of the NiCu cycle and its impact on modeling XRB observables.

I. INTRODUCTION

Type I X-ray bursts (XRBs) are the most frequent type of thermonuclear stellar explosions in the Galaxy. They are powered by thermonuclear runaways in hydrogen-and/or helium-rich material accreted onto the surface of a neutron star in a low-mass X-ray binary system. The main nuclear reaction flow in the XRB is driven toward the proton drip-line and to high masses via the triple-α reaction, a sequence of (α,p) and (p,γ) reactions (αp-process), and a series of (p,γ) reactions and β^+-decays (rp-process). Accurate nuclear physics inputs such as β decay rates, masses, and nuclear reaction rates of proton-rich rare isotopes along the path of the αp- and rp-processes are needed to model the energy production and nucleosynthesis in XRBs. Our understanding of XRBs has greatly expanded, yet many open questions still remain despite decades of work [1–3].

As indicated in Fig. 1, under XRB conditions, the rp-process beyond ^{56}Ni may be affected by several cycles. A low ^{59}Cu$(p,\gamma)^{60}$Zn rate or a high ^{59}Cu$(p,\alpha)^{56}$Ni rate would lead to the formation of a stronger NiCu cycle that returns the reaction flux to ^{56}Ni, which would strongly impede the synthesis of heavier nuclei and also affects the XRB observables [4]. The strength of the NiCu cycle is determined by the ratio of the (p,α) to (p,γ) reaction rates at ^{59}Cu. Currently, both rates recommended by REACLIB [5] are calculated by the Hauser-Feshbach statistical model [6, 7]. The variations in these rates have been identified as having a significant impact on

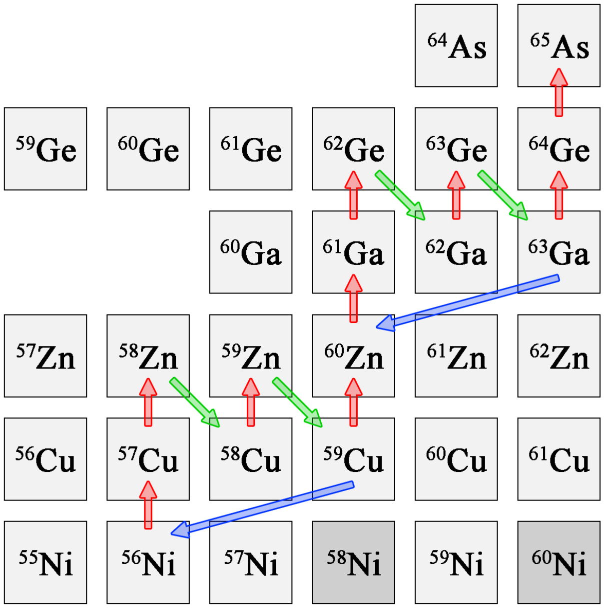

FIG. 1. Portion of the rp-process reaction sequence featuring the NiCu cycle and ZnGa cycle. ^{58}Ni and ^{60}Ni are stable.

---

[*] sunli@frib.msu.edu
[†] wrede@frib.msu.edu

the modeling of XRB light curves and the composition of the burst ashes [8–10]. The competition between ^{59}Cu$(p,\gamma)^{60}$Zn and ^{59}Cu$(p,\alpha)^{56}$Ni reactions at higher temperatures ($\sim$3 GK) is found to have a significant impact on the νp-process nucleosynthesis in core-collapse supernovae [11–13]

It is not currently possible to measure these two reactions at astrophysical energies directly because the predicted cross sections are too small, and intense low-energy radioactive ^{59}Cu beams are not available. A ^{59}Cu$(p,\alpha)^{56}$Ni reaction measurement using a ^{59}Cu beam with an intensity of 3600 particle per second (pps) and a cryogenic solid H_2 target at center-of-mass energy $E_{\mathrm{c.m.}} = 6.0$ MeV found that ^{59}Cu(p,α) proceeds predominantly to ^{56}Ni ground state, and standard statistical model calculations overestimate the cross section by a factor of $1.6-4$ [14]. In a ^{58}Ni$(^3$He$,n)^{60}$Zn reaction measurement [15], the nuclear level density of ^{60}Zn was extracted from the neutron evaporation spectrum. At an excitation energy of 6 MeV, the level density is estimated to be only $\sim$18 MeV^{-1}. The level density of ^{60}Zn resonances within the Gamow window may not be sufficiently high to justify a statistical treatment. Kim *et al.* [16] evaluated available experimental data on ^{60}Zn resonances, supplemented with theoretical calculations. They found the ^{59}Cu$(p,\alpha)^{56}$Ni reaction rate to be lower than the REACLIB rate [5] at XRB temperatures, implying a weaker NiCu cycle strength than previously estimated [8–10].

There are several ongoing efforts to address this problem, such as direct measuring the ^{56}Ni$(\alpha,p)^{59}$Cu reaction using a ^{56}Ni beam of 3000 pps on a He jet target [17], populating ^{60}Zn resonances via the ^{59}Cu$(d,n)^{60}$Zn transfer reaction [18] and via ^{60}Ga decay total absorption spectroscopy [19]. We also plan to identify resonances in ^{60}Zn via ^{60}Ga decay using the Gaseous Detector with Germanium Tagging [20]. To this day, experimental constraints on the ^{59}Cu$(p,\gamma)^{60}$Zn and ^{59}Cu$(p,\alpha)^{56}$Ni are still scarce and limit a robust understanding of their astrophysical impacts.

In the case of low level density in the compound nucleus, the narrow-resonance reaction rates can be calculated using the well-known relation [21],

$$N_A\langle\sigma\nu\rangle_r = 1.5394\times10^{11}(\mu T_9)^{-3/2}\times\omega\gamma \times\exp\left(-\frac{11.605E_r}{T_9}\right)(\mathrm{cm^3s^{-1}mol^{-1}}), \tag{1}$$

where $\mu = A_pA_T/(A_p+A_T)$ is the reduced mass in atomic mass units, with $A_p = 1$ and $A_T = 59$ as the mass numbers of proton and ^{59}Cu, respectively. E_r is the resonance energy in the center-of-mass system in units of MeV. T_9 is the temperature in units of giga kelvin (GK), and $\omega\gamma$ is the resonance strength in units of MeV. For the ^{59}Cu$(p,\gamma)^{60}$Zn resonance:

$$\omega\gamma = \frac{2J_r+1}{(2J_p+1)(2J_T+1)}\frac{\Gamma_p\Gamma_\gamma}{\Gamma_{\mathrm{tot}}}, \tag{2}$$

where J_r is the spin of the resonance, $J_p = 1/2$ is the spin of proton, and $J_T = 3/2$ is the spin of the ground state of ^{59}Cu. The total decay width Γ_{tot} of the resonance is the sum of the partial decay widths, including proton width (Γ_p), γ width (Γ_γ), and α width (Γ_α) for the resonances relevant to XRBs. Equivalently, the resonance strength can be constructed by combining the proton branching ratio $B_p = \Gamma_p/\Gamma_{\mathrm{tot}}$, the γ-ray branching ratio $B_\gamma = \Gamma_\gamma/\Gamma_{\mathrm{tot}}$, and the lifetime τ using the following expression:

$$\omega\gamma = \frac{2J_r+1}{(2J_p+1)(2J_T+1)}B_pB_\gamma\frac{\hbar}{\tau}, \tag{3}$$

where $\hbar$ is the reduced Planck constant. These relations are also applicable to the ^{59}Cu$(p,\alpha)^{56}$Ni resonance by replacing the terms Γ_γ and B_γ with Γ_α and B_α, respectively. Therefore, the useful nuclear physics inputs include the resonance energies, the spins, the proton, γ-ray, and α-decay branching ratios, and the lifetimes of the ^{60}Zn resonances.

The Gamow energies and windows for the ^{59}Cu$(p,\gamma)^{60}$Zn and ^{59}Cu$(p,\alpha)^{56}$Ni reactions shown in Table I are calculated from a numerical study of the relevant energy ranges for astrophysical reaction rates [22]. Discussing these two reactions at temperatures below 0.5 GK is not relevant as the abundance flow cannot reach this mass region [4, 47]. Combined with the proton-separation energy of ^{60}Zn $S_p(^{60}\mathrm{Zn}) = 5105.0(4)$ keV [23] and α-separation energy of ^{60}Zn $S_\alpha(^{60}\mathrm{Zn}) = 2691.7(5)$ keV [23], the excitation energies for ^{60}Zn resonances of interest range from 5.6 to 9.3 MeV, which are energetically accessible in ^{60}Ga β decay owing to the large $Q_{\mathrm{EC}}(^{60}\mathrm{Ga}) = 14161(15)$ keV [24, 25].

Table II summarizes the spins and parities of relevant ^{60}Zn resonances. It is evident that only positive parity states associated with $\ell = 1$ proton captures are accessible via allowed ^{60}Ga β transitions, also indicating that we will deal with an even lower level density in the β decay study than that the previous ^{58}Ni$(^3$He$,n)^{60}$Zn reaction measurement [15].

Fig. 2 summarizes currently known ^{60}Ga decay properties. ^{60}Ga is observed to decay by βp with an intensity of $I_p = 1.6(7)\%$ and possibly by $\beta\alpha$ with $I_\alpha \leq 0.023(20)\%$ [29]. When combined with the β-feeding intensities derived from the $\beta\gamma$-ray intensities reported by Refs. [24, 29], it is notable that approximately 26% of β-feeding intensities remain unaccounted for.

Coincidence measurements of all protons and γ rays emitted in ^{60}Ga β decay will construct a more complete decay scheme, including the proton-emitting states in ^{60}Zn and excited states and the ground state of ^{59}Cu.

TABLE I. Gamow windows $\widetilde{E}_{\mathrm{hi}} - \widetilde{\Delta} \leq E \leq \widetilde{E}_{\mathrm{hi}}$ and Gamow peaks $\widetilde{E}_0$ for the $^{59}\mathrm{Cu}(p,\gamma)^{60}\mathrm{Zn}$ and $^{59}\mathrm{Cu}(p,\alpha)^{56}\mathrm{Ni}$ reactions at a temperature T [22].

	$^{59}\mathrm{Cu}(p,\gamma)^{60}\mathrm{Zn}$			$^{59}\mathrm{Cu}(p,\alpha)^{56}\mathrm{Ni}$		
T (GK)	$\widetilde{E}_{\mathrm{hi}} - \widetilde{\Delta}$ (MeV)	$\widetilde{E}_0$ (MeV)	$\widetilde{E}_{\mathrm{hi}}$ (MeV)	$\widetilde{E}_{\mathrm{hi}} - \widetilde{\Delta}$ (MeV)	$\widetilde{E}_0$ (MeV)	$\widetilde{E}_{\mathrm{hi}}$ (MeV)
0.5	0.51	0.71	0.92	0.55	0.74	0.98
1.0	0.67	0.91	1.26	0.73	1.01	1.48
1.5	0.75	1.01	1.57	0.87	1.27	2.11
2.0	0.82	1.14	1.83	1.01	1.74	2.80
2.5	0.85	1.40	2.05	1.24	2.19	3.52
3.0	0.89	1.49	2.26	1.51	2.66	4.16

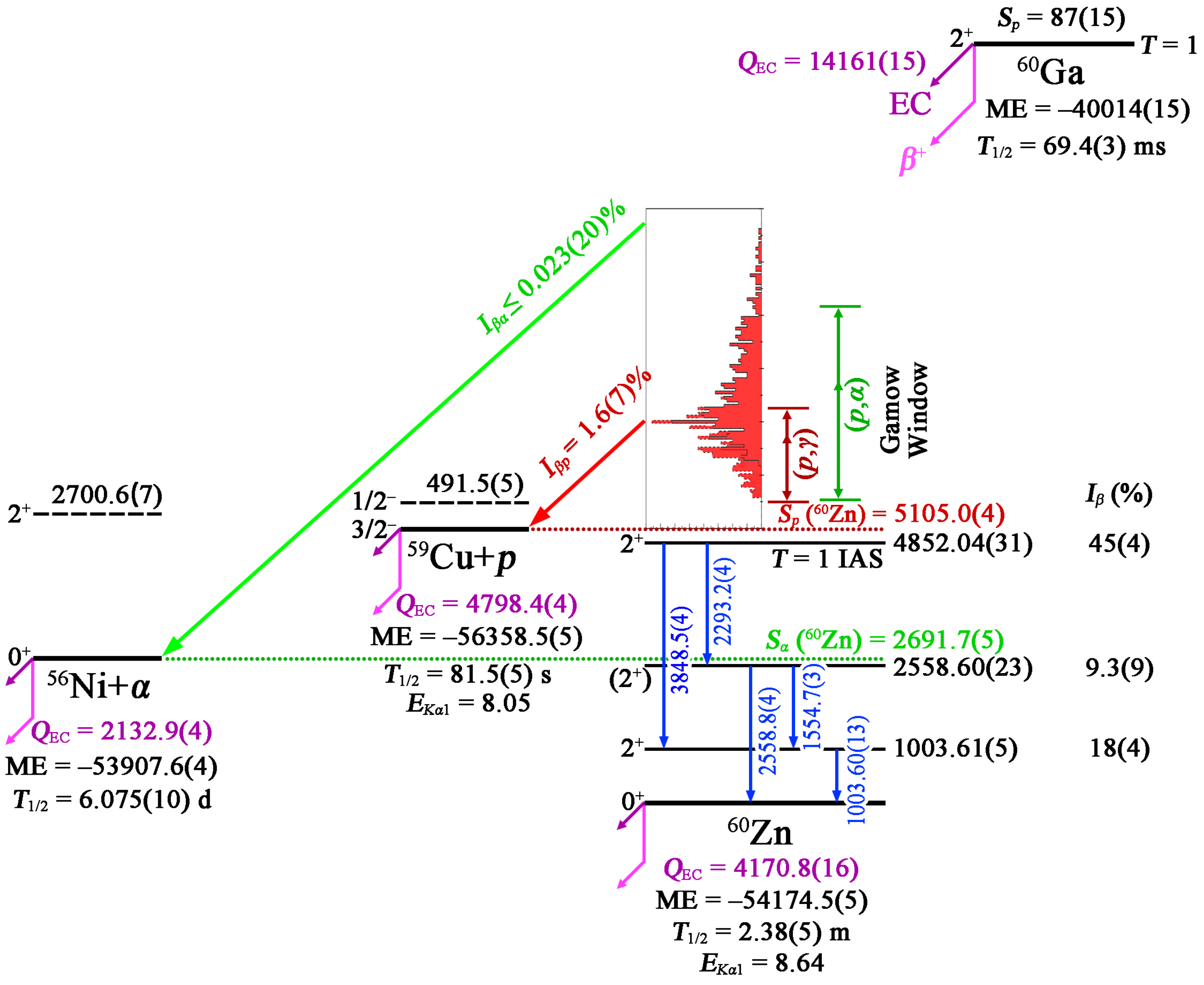

FIG. 2. Known decay scheme of ^{60}Ga. All energies are given in units of keV. The mass excesses, Q_{EC} values, and particle separation energies of ^{56}Ni, ^{59}Cu, and ^{60}Zn are from AME2020 [23], while for ^{60}Ga, these data are evaluated based on Refs. [24, 25]. The half-lives of ^{56}Ni, ^{59}Cu, and ^{60}Zn are from evaluations [26–28], respectively. The half-life of ^{60}Ga is evaluated based on Refs. [24, 29–31]. All spins and parities are adopted from evaluations [26–28], with the 4852-keV state in ^{60}Zn revised from (2^+) to 2^+ based on the unambiguous $T = 1$ isobaric analog state argument [24, 29]. The γ-ray energies, excitation energies, and β feedings of ^{60}Zn states are evaluated [32] based on all available measurements [24, 29, 33, 34]. The proton spectrum is extracted from only βp measurement [29]. The two dashed lines represent the first excited states of ^{56}Ni and ^{59}Cu, respectively, which have not been observed in ^{60}Ga decay. The double-headed arrows denote the Gamow windows for the $^{59}\mathrm{Cu}(p,\gamma)^{60}\mathrm{Zn}$ and $^{59}\mathrm{Cu}(p,\alpha)^{56}\mathrm{Ni}$ reactions at temperatures of 0.5–3 GK, respectively (Table I).

TABLE II. Properties of ^{60}Zn states populated via proton captures on the $3/2^-$ ^{59}Cu ground state and the $1/2^-$ ^{59}Cu first excited state, and the allowed β transitions of the 2^+ ^{60}Ga ground state.

Population	^{60}Zn states
$\ell = 0$ p on $3/2^-$	1^-, 2^-
$\ell = 1$ p on $3/2^-$	0^+, 1^+, 2^+, 3^+
$\ell = 2$ p on $3/2^-$	0^-, 1^-, 2^-, 3^-, 4^-
$\ell = 0$ p on $1/2^-$	0^-, 1^-
$\ell = 1$ p on $1/2^-$	0^+, 1^+, 2^+
$\ell = 2$ p on $1/2^-$	1^-, 2^-, 3^-
β transition from 2^+	1^+, 2^+, 3^+

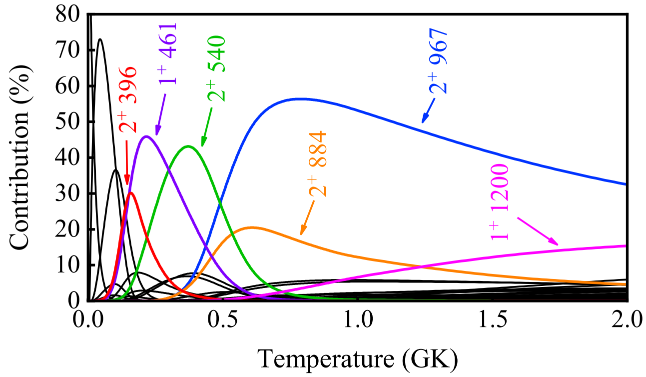

FIG. 3. ^{59}Cu$(p,\gamma)^{60}$Zn reaction rate contribution from 66 resonances predicted by the shell model. The key resonances are highlighted with their spin, parity, and resonance energy.

This will provide valuable information on the entrance and exit channels for relevant thermonuclear reactions.

To identify potentially important resonances, we performed shell-model calculations in the truncated fp-shell model space with the GPFX1A Hamiltonian [35] using the NuShellX@MSU code [36]. The newly-evaluated ^{60}Ga $Q_{\mathrm{EC}} = 14161(15)$ keV was incorporated into the calculation. We obtained 900 ^{60}Zn states up to $E_x = 12.6$ MeV, with 300 states each for $J^\pi = 1^+, 2^+, 3^+$. A quenching factor $q^2 = 0.6$ for the matrix elements of the Gamow-Teller operator was used to calculate the β-feedings in ^{60}Ga decay. We also calculated the partial decay widths Γ_p and Γ_γ for 66 resonances with $J^\pi = 1^+, 2^+, 3^+, 4^+, 5^+$ up to $E_x = 6.5$ MeV. The total widths were supplemented by interpolating the average Γ_α values calculated using the statistical model code NON-SMOKER [6]. The statistical model shows that ^{60}Zn states with negative parity are all above $E_x = 6.8$ MeV, which implies that they are less likely to contribute significantly to the total reaction rate. We calculated the ^{59}Cu$(p,\gamma)^{60}$Zn reaction rate by combining all 66 positive parity resonances, and the fractional contributions of each resonance are shown in Fig. 3. Table III summarizes the properties of the six most influential resonances. Notably, over the XRB temperature range of 0.5−1.5 GK, a single resonance at $E_r = 967$ keV dominates the total rate. If only a handful of key ^{60}Zn resonances exist, and we can identify them through ^{60}Ga β decay, both the ^{59}Cu$(p,\gamma)^{60}$Zn and ^{59}Cu$(p,\gamma)^{60}$Zn reaction rates may be constrained.

TABLE III. Properties of potentially important ^{59}Cu$(p,\gamma)^{60}$Zn resonances predicted by shell model. The values in the first through tenth columns represent the spin and parity (J^{π}), the excitation energy (E_x), the resonance energy (E_r), the partial decay widths (Γ_γ, Γ_p, Γ_α), the lifetime (τ), the log ft value and the β-feeding intensity (I_β) for ^{60}Ga decay, and the ratio of EC/$\beta+$ feeding [37].

J^{π}	E_x (keV)	E_r (keV)	Γ_γ (eV)	Γ_p (eV)	Γ_α (eV)	τ (fs)	log ft	I_β (%)	$R_{\mathrm{EC}/\beta+}$
2^+	5501	396	3.9×10^{-2}	4.4×10^{-10}	2.9×10^{-7}	16.9	5.463	0.314	1.6×10^{-3}
1^+	5566	461	4.4×10^{-1}	8.6×10^{-8}	0	1.5	4.708	1.713	1.6×10^{-3}
2^+	5645	540	2.0×10^{-1}	1.2×10^{-6}	1.1×10^{-6}	3.3	6.146	0.060	1.7×10^{-3}
2^+	5989	884	2.9×10^{-2}	2.9×10^{-3}	1.6×10^{-5}	20.6	5.367	0.287	1.9×10^{-3}
2^+	6072	967	2.5×10^{-1}	3.5×10^{-2}	2.9×10^{-5}	2.3	5.536	0.184	2.0×10^{-3}
1^+	6305	1200	3.8×10^{-1}	1.3×10^{-1}	1.3×10^{-27}	1.3	7.035	0.005	2.2×10^{-3}

II. PARTICLE X-RAY COINCIDENCE TECHNIQUE

In the 1970s, the Particle X-ray Coincidence Technique (PXCT) was introduced and applied to measure the average lifetimes of proton-unbound states in ^{69}As populated by the electron capture (EC) of ^{69}Se [38]. The principle of the method is illustrated in Fig. 4. In the process of an EC-delayed proton emission, a proton-rich precursor with an atomic number of Z decays by K-EC to the proton emitter $(Z-1)$. Due to the EC, a proton unbound nuclear state and an atomic shell vacancy are created simultaneously. An electron in a higher-lying atomic shell fills the vacancy with typical lifetimes of $\tau_{K\mathrm{shell}} = 0.01$ to 1.0 fs and emits the characteristic X ray. Meanwhile, the proton-unbound state with a comparable lifetime $\tau_{p-\mathrm{emit}}$ emits a proton to a state of the daughter $(Z-2)$. If the proton is emitted before the X-ray emission, then the X-ray energy will correspond to the atomic number of the daughter $(Z-2)$. If the proton is emitted after the X-ray emission, then the X-ray energy will be characteristic of the atomic number of the proton emitter $(Z-1)$. By measuring X rays in coincidence with protons, the relative intensities of the $(Z-1)$ and $(Z-2)$ X-ray peaks $I_{KX(Z-1)}/I_{KX(Z-2)}$ correcting for the radiative yields can be used to establish the relationship between the lifetimes of proton-emitting states and the lifetimes of the emitter K-shell vacancies:

$$\frac{\tau_{p-\mathrm{emit}}}{\tau_{K\mathrm{shell}}} = \frac{\Gamma_{K\mathrm{shell}}}{\Gamma_{p-\mathrm{emit}}} = \frac{I_{KX(Z-1)}}{I_{KX(Z-2)}}, \tag{4}$$

where the decay width $\Gamma_{K\mathrm{shell}}$ and $\Gamma_{p-\mathrm{emit}}$ is the equivalent of $\hbar/\tau_{K\mathrm{shell}}$ and $\hbar/\tau_{p-\mathrm{emit}}$, respectively, as they both follow the exponential decay law. Because the K-shell vacancy lifetimes are well known both experimentally and theoretically, ranging from $\tau \approx 2\times10^{-15}$ s for carbon down to $\tau \approx 6\times10^{-18}$ s for uranium [39, 40], lifetimes of proton-emitting states can be determined by measuring X-ray peak ratios. The preceding discussion is also generalizable to EC-delayed α-particle emission.

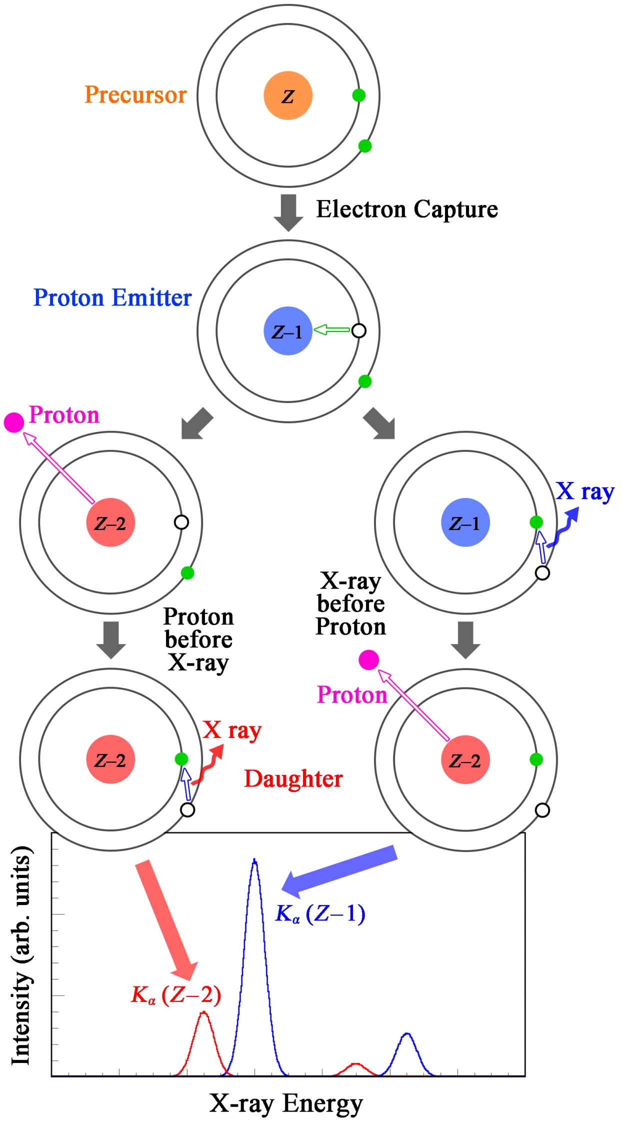

FIG. 4. Schematic illustrating the Particle-X-ray Coincidence Technique. See text for details.

TABLE IV. Properties of all nuclei that have been measured with PXCT. Columns 1−5 list the EC/β^+-decay precursors, the half-lives ($T_{1/2}$), the β-decay energies ($Q_{\rm EC}$), the proton-separation energies of the EC/β^+-decay daughters (S_p), and the total intensities of EC/β^+-delayed protons (I_p), respectively.

Precursor	$T_{1/2}$ (s)	$Q_{\rm EC}$ (keV)	S_p (keV)	I_p (%)	Literature
^{65}Ge	30.9(5)	6179.3(23)	3942.4(6)	0.011(3)	[41]
^{69}Se	27.4(2)	6680(30)	3420(30)	0.045(10)	[41, 42]
^{73}Kr	27.3(10)	7094(9)	3067(7)	0.25(3)	[41, 43, 44]
^{77}Sr	9.0(2)	7027(8)	3106(4)	0.08(3)	[41]
^{113}Xe	2.74(8)	8916(11)	841(12)	7(4)	[45]
^{117}Ba	1.75(7)	9040(260)	740(60)	16(3)	[46]

So far, the PXCT has been applied in six decay measurements, as summarized in Table IV. In all these cases, only the average sub-fs lifetimes of proton-unbound states populated by EC were obtained. Individual proton-emitting states could not be distinguished due to high level densities. Additionally, the applicability of this technique has not been explored in an astrophysical context. We have designed and built a detection system to extend the PXCT to measure both the lifetimes and branching ratios of individual resonances that are important for modeling explosive astrophysical scenarios.

Even if the level density of ^{60}Zn selected by β decay is still too high for us to resolve individual resonances, we can perform statistical analysis to extract the particle and γ-transmission coefficients and the nuclear level density of excited states [41], which are essential ingredients for calculating reaction rates within the statistical model [6]. The PXCT applied to ^{60}Ga EC/β^+ decay offers the unique advantage of obtaining all necessary quantities in a single experiment, rather than relying on separate measurements for different nuclear inputs.

III. EXPERIMENTAL SETUP

A. Beam delivery

The Facility for Rare Isotope Beams (FRIB) linear accelerator [48] will accelerate ^{70}Ge or ^{78}Kr to 256 MeV/u with a beam power up to 400 kW. The reaction products from ^{70}Ge or ^{78}Kr impinging on a rotating carbon target will be separated by the Advanced Rare Isotope Separator [49]. A cocktail fast beam containing ^{60}Ga and some nearby isotones will be slowed down in metal degraders with momentum compression and thermalized in gas stoppers filled with helium [50, 51]. The thermalized ^{60}Ga ions will drift towards a nozzle and exit into a radio-frequency quadrupole ion-guide system. The ions will be guided and accelerated to 30 keV through a combination of radio-frequency and direct-current fields before being delivered to the stopped beam area [52]. The intensity of the ^{60}Ga stopped beam is estimated to be up to 9×10^3 pps.

As shown in Fig. 5, we have designed and built a PXCT detection system that will be used in the stopped beam area. The experiment will start by tuning a stable beam around the $A = 60$ region into the Faraday cup at the center of the vacuum chamber. After maximizing the beam current, we will vent the chamber and replace the Faraday cup with an aluminized Mylar foil tilted at a 45° angle with respect to the beam direction. The ^{60}Ga beam will then be directed into the chamber. A 30-keV ^{60}Ga beam can be fully stopped by a Mylar foil as thin as 50 nm, in contrast to the 6.5 mm needed to stop the 130-MeV/u ^{60}Ga fast beam, which would block the emitted X rays and charged particles. The detection system comprises a silicon detector telescope for charged-particle detection via energy-loss and residual energy (ΔE-E), a planar germanium detector for X-ray detection, and two large-volume coaxial germanium detectors for γ-ray detection. The detection setup can provide real-time signals on characteristic charged particles and γ rays from decay, facilitating online beam optimization.

B. Detectors

For the ΔE-E charged-particle telescope, we selected two single-sided, single-area circular Si detectors manufactured by Micron Semiconductor Ltd. The active area of MSD12 is 12 μm thick and 12 mm in diameter [53], and MSD26 is 1000 μm thick and 26 mm in diameter [54]. The junction side of both MSDs features a 50-nm thick boron-doped silicon dead layer and a 30-μm wide peripheral metal band for wire bonding, leaving the majority of the active area without metal coverage. The Ohmic side of MSD12 has a thicker dead layer of 300 nm with no metal coverage. The Ohmic side of MSD26 has little impact on charged-particle signals, and thus, we opt for the standard 500-nm thick dead layer and 300-nm thick aluminum coverage. Both silicon chips are assembled onto an FR4 printed circuit board. MSD26 is positioned 15.7 mm from the center of the chamber and covers 11.5% of the 4π solid angle. MSD12 is 11.2 mm from the center and defines the solid angle coverage of the ΔE-E telescope at 5.9% of 4π.

For X-ray detection, we selected a Low Energy Germanium detector (LEGe), Mirion GL0510 [55]. The LEGe detector consists of a Ge crystal with a diameter of 25.0 mm and a length of 10.5 mm. LEGe is housed in a flanged-style cryostat with a diameter of 38.1 mm and a 0.13-mm thick beryllium entrance window. The endcap is inserted into the vacuum chamber with its entrance window 11.0 mm from the center of the chamber. The Ge crystal is positioned 5.6 mm from the entrance window, subtending 10.1% of the 4π solid angle. LEGe is fabricated with a thin p^+ contact on the front and side,

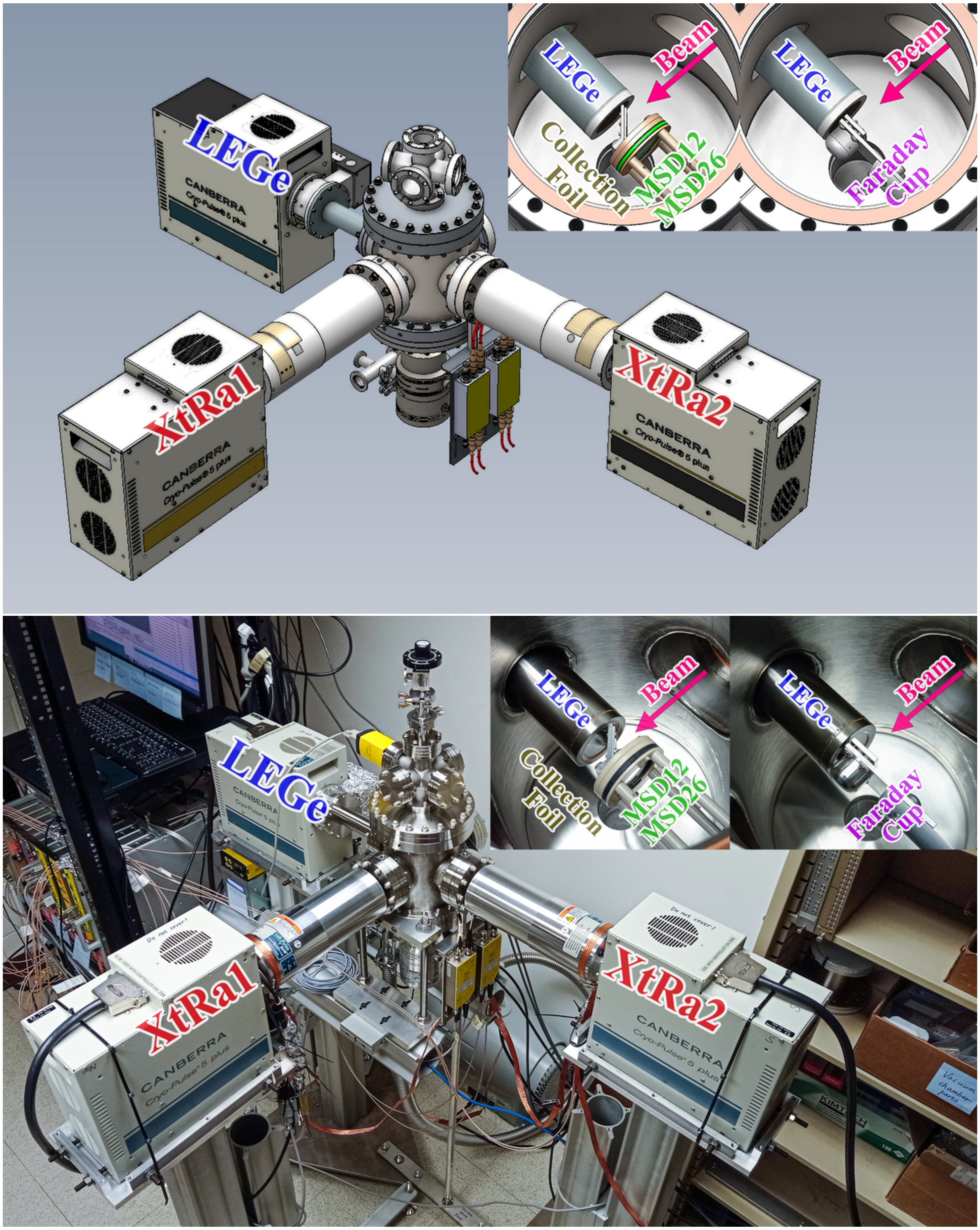

FIG. 5. Mechanical design drawing and photograph of the PXCT detection system. The insets highlight two configurations for the detectors inside the central chamber: a Faraday cup with a collimator for beam tuning or a collection foil and Si detectors for decay measurements.

and a rear n^+ contact that covers less than the full area, resulting in lower capacitance than a similar-sized planar device. Since preamplifier noise is a function of detector capacitance, the low capacitance feature makes LEGe ideally suited for X-ray spectroscopy down to 3 keV.

For γ-ray detection, we selected two Extended Range Coaxial Germanium Detectors (XtRa), Mirion GX10020 [56]. The active volume of XtRa1 has a diameter of 84.8 mm and a thickness of 65.2 mm, while XtRa2 has a diameter of 79.8 mm and a thickness of 80.0 mm. The Ge crystals are positioned 6.8 and 6.3 mm, respectively, from the 0.6-mm-thick carbon composite windows. XtRa detectors feature a thin window contact on the front surface and a n^+ contact on the side, providing a good low-energy response.

All three Ge detectors are equipped with the Cryo-Pulse 5 Plus (CP5-Plus) electrically refrigerated cryostat [57]. The detector housing is connected to a compact cold-head assembly containing a 5-watt pulse tube cooler. The assembly is powered by a bench-top controller, which includes a control panel application for remote monitoring and safe operation of the cryostat.

C. Electronics

All three Ge detectors are equipped with the Intelligent Preamplifiers (iPA) [59], which incorporate a low-noise field-effect transistor (FET) input circuit optimized for the ultra-high source impedance of Ge detectors. The first stage of the iPA functions as an integrator and an electrometer, providing an output voltage proportional to the accumulated charge and measuring the leakage current. The second stage of the iPA acts as an output buffer and provides four selectable gain settings. The iPA also enables remote monitoring of detector current, temperatures, and preamplifier operating voltages. In the event that the temperature exceeds the normal operating range, warm-up sensors trigger a high-voltage inhibit signal from the preamplifier and the controller, respectively, thereby protecting the Ge crystals.

Two ORTEC 660 Dual Bias Supply modules [60] are used to provide bias voltages to the three Ge detectors. We apply a negative bias to the p^+ contacts of LEGe and a positive bias to the n^+ contacts of XtRa. LEGe becomes fully depleted at -600 V and is recommended to be operated at -1100 V. XtRa1 and XtRa2 become fully depleted at a bias voltage of $+4000$ V and $+2200$ V, respectively, and both operate at $+4500$ V. ORTEC 660 includes a remote bias shutdown feature to protect the preamplifier FET against damage in the instance of accidental warm-up of the Ge detector. The typical leakage currents of the two XtRa detectors are below 20 pA and below 100 pA for LEGe. A Mesytec MHV 4-channel bias supply module with remote control features provides the bias voltages to the two MSD Si detectors. We apply a negative bias to the p^+ contacts of both MSD detectors through MPR-1 charge-sensitive preamplifiers [61] and the n^+ contacts are grounded. MSD12 has a depletion voltage of -1.5 V and is operated at -3.0 V, and MSD26 has a -90 V depletion voltage and is operated at -130 V. MHV offers a ramp speed as low as 5 V/s to protect the circuits of preamplifiers [62]. MSD26 has a leakage current of approximately 60 nA, whereas MSD12 maintains a leakage current below 1 nA. All the preamplifiers are powered by two Mesytec MNV-4 NIM power distribution and control modules [63].

D. Data acquisition

All the preamplifier signals are transmitted via double-shielded RG316 coaxial cables of equal length and then digitized by a 16-bit, 250 MHz Pixie-16 module manufactured by XIA LLC [64]. The input impedance of each channel in Pixie-16 is configured to be 1 kΩ. The Digital Data Acquisition System (DDAS) is used [65, 66] for recording and processing data. Trapezoidal filtering algorithms are implemented in both the slow filter for pulse amplitude measurement and the fast filter for leading-edge triggering. Each event is timestamped using a Constant Fraction Discriminator (CFD) algorithm based on the trigger filter response. The system operates in an internally triggered mode: recording data on a channel-by-channel basis whenever the trigger filter crosses the user-defined threshold. The data from all channels is ordered in time and subsequently assembled into events based on a user-defined event window length. The event timestamp is counted with 125 MHz clock ticks, i.e., 8 ns intervals.

The tail pulses from MPR-1 exhibit rise times of 400 ns (MSD12) and 70 ns (MSD26), with a 120 μs decay constant. The tail pulses from iPA exhibit rise times of 150 ns (LEGe) and 250 ns (XtRa), with a 50 μs decay constant. The DDAS filter parameters are optimized based on these observations [66–69]. The pulse amplitude is extracted from the energy filter amplitude at approximately rise time plus gap time after triggering. If a second trigger arrives within the rise time plus gap time window, both events will be flagged as pile-up. The energy filter parameters are the dominant factor in determining the count rate capacity of the DDAS system.

IV. PERFORMANCE TESTS

We have performed comprehensive tests on the PXCT system using the electronics configuration illustrated in Fig. 6.

A DB-2 Random Pulser [70] was used to investigate the data acquisition dead time. The time intervals between successive pulses follow a Poisson distribution function. The count rate performance is shown in Fig. 7. The observed event losses are in line with the pile-up rates defined by the energy filter settings [65]. Considering the achievable stopped beam rates at FRIB,

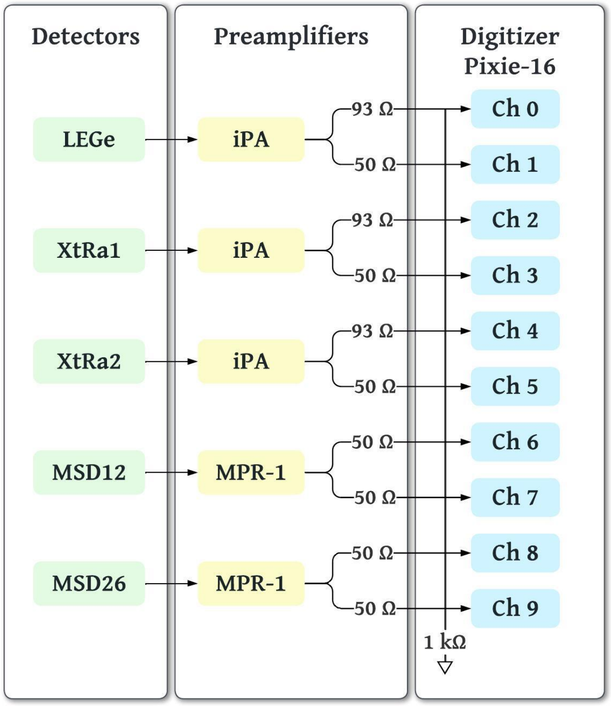

FIG. 6. Schematic diagram of the electronics setup. The two arrows following each preamplifier indicate dual outputs with their respective impedance.

decay observables, and detection efficiencies, no detector will need to process more than 1000 events per second in the ^{60}Ga decay experiment.

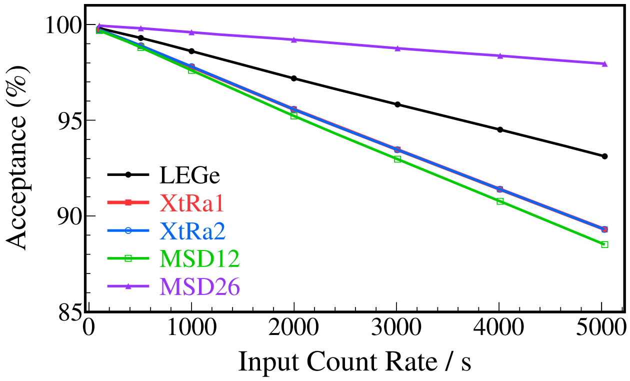

FIG. 7. DDAS count rate performance.

Table V lists the characteristics of all radioactive sources used in the PXCT detector tests. A typical event-build window of ±1 μs was used, and the count rate of each detector remained below 1500 events per second throughout all conducted tests, except for the LEGe efficiency test with the ^{152}Eu source.

TABLE V. Radioactive sources used in the PXCT detector tests. Columns one through six display the source numbers, source nuclides, actual activities, relative uncertainties of the activities, active diameters, and half-lives, respectively. Source No. 6 does not generate measurable α particles and is only used for LEGe testing. The ^{241}Am source in all the other tests refers to Source No. 7. A hyphen (−) is placed where the information is unavailable

No.	Nuclide	A (Bq)	σA (%)	D (mm)	$T_{1/2}$ (y)
1	^{55}Fe	1.11×10^4	−	9.5	2.74
2	^{60}Co	3.73×10^4	3	1	5.27
3	^{137}Cs	3.00×10^3	3	−	30.1
4	^{148}Gd	2.86×10^4	−	5	71.1
5	^{152}Eu	3.10×10^4	1.4	3	13.5
6	^{241}Am	3.65×10^5	3.6	3.0	432.6
7	^{241}Am	3.44×10^3	2.7	3.2	432.6

A. X-ray measurements

We evaluated the performance of LEGe using the X rays and low-energy γ rays from the ^{55}Fe, ^{152}Eu, and ^{241}Am sources, as shown in Fig. 8. The overall energy resolution achieved by LEGe is characterized by fitting known X-ray or γ-ray lines with an exponentially modified Gaussian (EMG) function to account for incomplete charge collection [71] at 5.90 keV (Mn $K_{\alpha1}$), 6.49 keV (Mn $K_{\beta1}$), 11.89 keV (Np L_ℓ), 13.76 keV (Np $L_{\alpha2}$), 13.95 keV (Np $L_{\alpha1}$), 26.34 keV (^{237}Np γ), 33.20 keV (^{237}Np γ), 39.52 keV (Sm $K_{\alpha2}$), 40.12 keV (Sm $K_{\alpha1}$), 45.29 keV (Sm $K_{\beta3}$), 45.41 keV (Sm $K_{\beta1}$), and 59.54 keV (^{237}Np γ). We then interpolated the full width at half maximum (FWHM) values at the energies of interest, 8.05 keV (Cu $K_{\alpha1}$) and 8.64 keV (Zn $K_{\alpha1}$), to be 0.238(8) and 0.241(7) keV, respectively, demonstrating sufficient resolution to distinguish between the key X rays of Zn and Cu.

For photons below 100 keV interacting with Ge, the photoelectric effect is predominant, i.e., the photon is absorbed, and its energy is transferred to an electron and causes prompt emission of a characteristic X ray as the resulting vacancy in the electron shell is filled. A full-energy peak is still observed if this X ray is reabsorbed near the original interaction site. However, if the photoelectric interaction occurs near the surface of Ge, the X ray is more likely to escape, which results in peaks usually at 9.89 keV and 10.98 keV below the photopeaks, known as the Ge escape peaks (Fig. 8). These energy differences correspond to the characteristic $K_{\alpha1}$ and $K_{\beta1}$ X-ray energies for Ge, respectively [72].

We evaluated the detection efficiency of LEGe using the X rays from the ^{152}Eu source placed at the center of the chamber tilted at a 45° angle with respect to LEGe. ^{152}Eu emits Sm L X rays at 5.0 keV (L_ℓ), 5.6 keV (L_η, L_α), 6.2 keV (L_β), and 7.2 keV (L_γ). The Gd L X rays

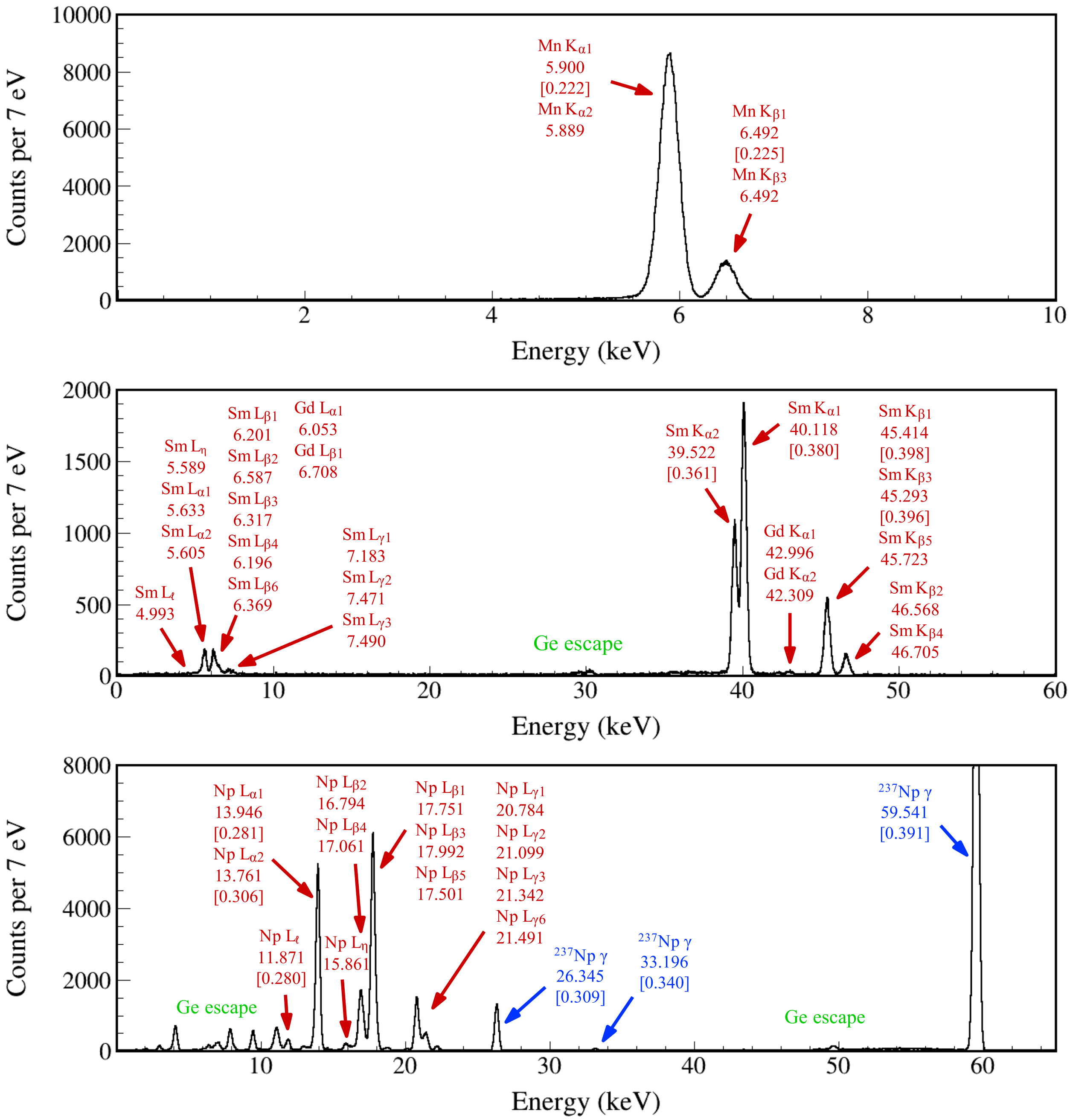

FIG. 8. X-ray and/or γ-ray spectra measured by the LEGe detector using the ^{55}Fe (top), ^{152}Eu (middle), and ^{241}Am (bottom) sources. All the X-ray energy values are adopted from Ref. [72] rounded to the nearest 0.01 keV. All the γ-ray energy values are adopted from Ref. [75] rounded to the nearest 0.01 keV. The FWHM values used to characterize the energy resolution of LEGe are indicated within brackets.

are approximately half a keV higher but with two orders of magnitude lower intensities. We adopted the total L X-ray emission probability from Ref. [73] and deduced the absolute intensity for each of the 4 groups of X rays based on the relative emission probabilities reported by Ref. [74]. The corresponding efficiencies are indicated by the 4 low-energy data points in Fig. 9. We also measured the X rays from the ^{241}Am source placed at the center of the chamber. ^{241}Am emits Np L X rays at 11.9 keV (L_ℓ), 13.9 keV (L_α), 15.9 keV (L_η), and 17.0 keV (L_β). The corresponding efficiencies are indicated by the 4 high-energy data points in Fig. 9. We simulated the X-ray detection efficiencies using GEANT4 [78, 79]. The simulation incorporates the geometric configuration of the setup and the LEGe detector response, which was characterized by fitting the measured X-ray lineshapes in Fig. 8 with the EMG function. Monoenergetic X rays are emitted isotropically from the source position and interact with the surrounding materials. The simulation outputs an energy spectrum, from which we obtain the detection efficiency by dividing the counts in the X-ray peak by the number of emitted X rays. This process was repeated at different energies to generate the efficiency curves shown in Fig. 9.

For photon energies just above the K-shell binding energy of Ge, 11.1030(20) keV [72], the incident photon is strongly absorbed without deep penetration beyond the detector surface. The subsequent characteristic K X rays of 9.7−11.1 keV tend to escape, thereby decreasing the full energy peak efficiency. This phenomenon can potentially complicate the detection efficiency of near-edge X rays. However, for the energies of interest at 8−9 keV, K-shell absorption is no longer possible, and L-shell interactions dominate. In this case, incident γ rays tend to penetrate somewhat deeper, and the chance of escape of the fluorescent Ge L X rays of 1.0−1.4 keV is significantly lower. The ^{241}Am source used for this test is an open source, while the ^{152}Eu source is encapsulated between two 60-μm thick Mylar tapes. The Mylar layer attenuates low-energy X-rays, but its impact diminishes for X rays exceeding 10 keV. Additionally, the LEGe count rate was ∼3000 pps during the ^{152}Eu test but only ∼200 pps during the ^{241}Am test, resulting in different DAQ dead time (Fig. 7). Therefore, the ^{152}Eu efficiency curve represents a lower limit, while the ^{241}Am efficiency curve represents an ideal setting. The ^{60}Ga experimental condition is expected to fall between these two scenarios, and we estimate the X-ray efficiencies at 8.0 and 8.6 keV to be 6.5−7.4% and 7.0−7.8%, respectively.

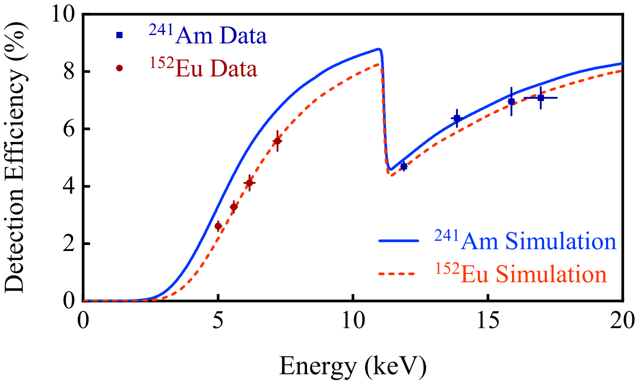

FIG. 9. Absolute X-ray photopeak detection efficiency of the LEGe detector obtained using the Sm L_ℓ, $L_\eta + L_\alpha$, L_β, and L_γ X rays from the ^{152}Eu source and Np L_ℓ, L_α, L_η, and L_β X rays from the ^{241}Am source, each placed at the center of the chamber. The red dashed and blue solid curves represent the GEANT4 simulated efficiencies according to the ^{152}Eu and ^{241}Am source configurations, respectively. The error bars along the x-axis also reflect the energy span for the multiple X rays within each group.

B. γ-ray measurements

Figure 10 shows the γ-ray spectra measured by XtRa1 and XtRa2 using the ^{152}Eu source. We first placed the source at the midpoint between the two XtRa detectors that were facing each other, with a distance of 28 cm between them. Both XtRa detectors exhibit good low-energy response to the ^{152}Sm X rays at 40 keV. We then placed the source at the center of the vacuum chamber to determine the absolute γ-ray detection efficiencies. The two XtRa detectors were placed as close as possible to the two flanges (Fig. 5), with their entrance windows about 12 mm from the flange surface. XtRa1 Ge crystal has a slightly larger diameter than XtRa2. Both Ge crystals are 158.5 mm from the target center, covering 1.70% and 1.51% of the 4π solid angle, respectively. Both XtRa detectors record an average of 300 room background gamma rays per second in our lab test environment. The achieved energy resolution aligns with the specifications provided by the manufacturer. The absence of X-ray peaks in the second test (lower panel of Fig. 10) is due to the 3.175-mm thick stainless steel flanges of the chamber effectively blocking the X rays.

We also measured the γ-ray detection efficiencies using the ^{60}Co and ^{137}Cs sources placed at the center of the chamber. MSD12 was not in place during these tests due to its fragility. MSD26 and the Si detector holders attenuated the γ rays from the source to XtRa2 but had little effect on XtRa1. Based on an exponential function [77] that contains a polynomial of degree i with the natural logarithm of the energy E: $\varepsilon(E) = \exp\left[\sum_{i=0}^{6} p_i \ln(E)^i\right]$ fit on all the data points, we obtain the photopeak efficiencies of 0.334(3)% and 0.286(3)% at 1 MeV, respectively, for XtRa1 and XtRa2. The error bars on the data points reflect the uncertainty of the γ-ray yields and the source activities, with an additional 2.5% to account for the true coincidence summing effect.

We have used GEANT4 simulation [78, 79] to extend the γ-ray detection efficiency curve to high energies (Fig. 11). The simulation takes into account the geometry of the setup and the detector response characterized by fitting the measured γ-ray lineshapes with the EMG function. Monoenergetic γ rays were emitted isotropically according to the source distribution and interacted with the surrounding materials. The photopeak efficiency was extracted from the output spectrum. We then fit the ratio of the simulated efficiency to the measured efficiency between 0.5−1.5 MeV and obtained energy-independent ratios of 0.875(10) and 0.837(10) for XtRa1 and XtRa2, respectively, which serve as the normalization factors to match the simulation with the experimental data. One of the factors that reduces the measured efficiency is the data acquisition event loss, which is estimated to be 2−5% based on the count rates during these tests (Fig. 7).

The mechanical design allows for the versatile combination of individual detectors for various

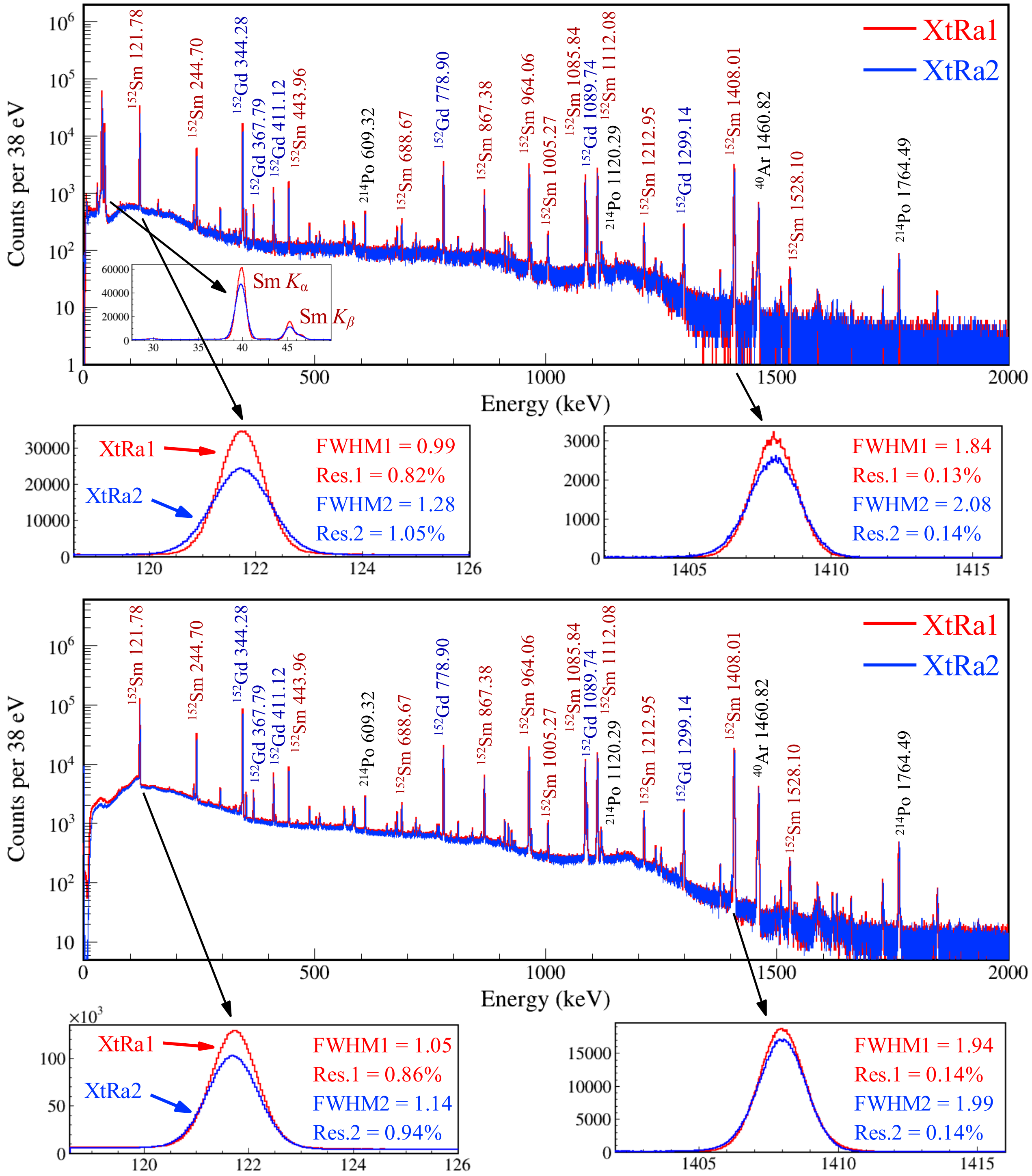

FIG. 10. γ-ray spectra measured by XtRa1 (red) and XtRa2 (blue) using the ^{152}Eu source. Upper panel: the ^{152}Eu source is placed in the middle of the two XtRa facing each other. Lower panel: the ^{152}Eu source is placed at the center of the vacuum chamber, with the two XtRa detectors positioned according to the Fig. 5 configuration. All the γ-ray energy values are adopted from Ref. [76] rounded to the nearest 0.01 keV. The insets demonstrate the detector responses at 122 and 1408 keV.

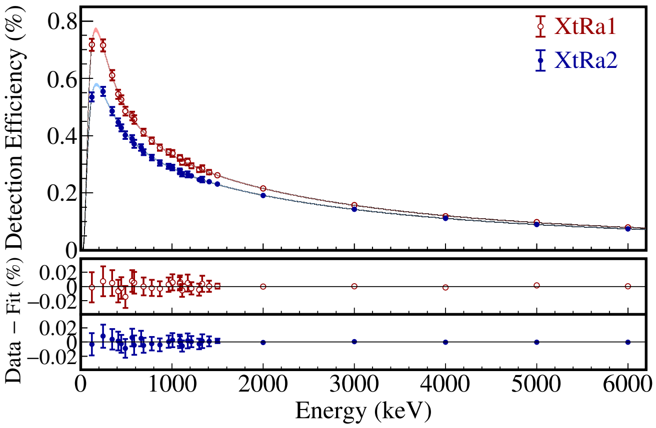

FIG. 11. Absolute γ-ray photopeak detection efficiency of the two XtRa detectors obtained using the ^{152}Eu, ^{137}Cs, and ^{60}Co sources placed at the center of the chamber. The ^{137}Cs data point at 662 keV is only applicable to XtRa2 due to the source placement. The 6 data points above 1408 keV are GEANT4 simulated efficiencies scaled by a factor to match the low-energy source data. The efficiency curves are generated by fitting all measured and simulated data points.

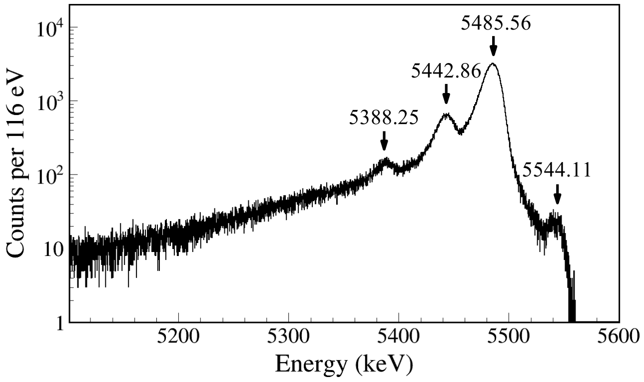

FIG. 12. α spectrum measured by MSD26 using the ^{241}Am source. The α energy values are adopted from Ref. [83] rounded to the nearest 0.01 keV. An EMG fit of the main peak yields the FWHM value to be 17.0 keV, corresponding to an energy resolution of 0.31%.

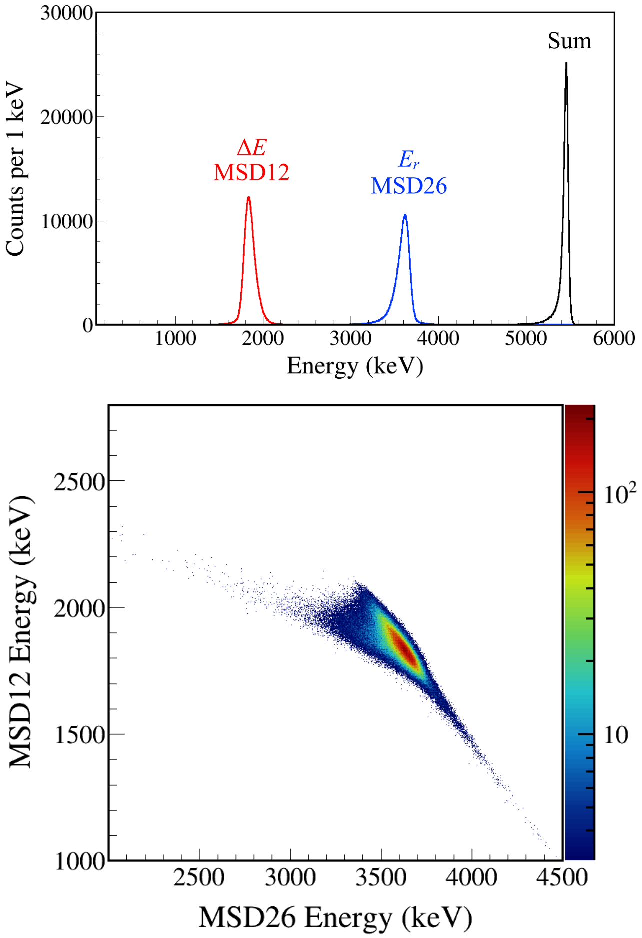

FIG. 13. Upper: ^{241}Am α-energy spectra measured by MSD12 (energy-loss) and MSD26 (residual energy). An EMG fit of the energy-sum peak yields a FWHM of 52.1 keV, corresponding to an energy resolution of 0.95%. Lower: ΔE-E 2D plot.

experimental purposes. The two XtRa detectors have been coupled with a silicon cube [80] and with a Time Projection Chamber [20]. We also have the option to integrate LEGe and the central chamber with larger Germanium detector arrays, such as the DEcay Germanium Array initiator [81], to achieve a higher γ-ray detection efficiency.

C. Charged-particle measurements

Figure 12 shows the α spectrum measured by MSD26 alone using the ^{241}Am source, with a 2-mm diameter aperture installed in front. MSD12 alone is too thin to stop α particles above 3 MeV, and we demonstrate the ΔE-E α spectra measured by the telescope formed by MSD12 and MSD26 in Fig. 13. The α sum peak exhibits an energy resolution of 0.95%. We first installed MSD26 and calibrated it using the ^{148}Gd (E_α = 3182.68 keV [82]) and ^{241}Am sources, and then measured the residual energy of ^{241}Am α particles in MSD26 with MSD12 installed in front of it. This allowed us to accurately determine the effective thickness of MSD12 to be 11.65(8) μm after subtracting the 0.35-μm dead layer thickness. The total thickness of MSD12 is in agreement with the nominal value of 12 μm specified in the Micron datasheet.

D. Coincidence measurements

Figure 14 shows the α-γ coincidence spectrum between the MSD telescope and LEGe with the ^{241}Am source placed at the center of the chamber. The majority of low-energy photons emitted from ^{241}Am are attenuated by the source substrate, leaving only the 59.5-keV γ ray in ^{237}Np and its escape peaks noticeable.

Since there are no suitable radioactive sources for us to directly measure proton-X-ray coincidences, we simulated proton and α spectra observed by the ΔE-E telescope and proton-gated X-ray spectrum observed by LEGe using GEANT4. The simulation takes into account the theoretical ^{60}Ga decay scheme, the measured detector responses, and the estimated statistics with achievable ^{60}Ga beam intensity in one week. Figure xx demonstrates the system is able to resolve individual resonances. The inset highlights the 967-keV proton-gated X-ray spectrum, from which the lifetime of the 967-keV resonance can be obtained.

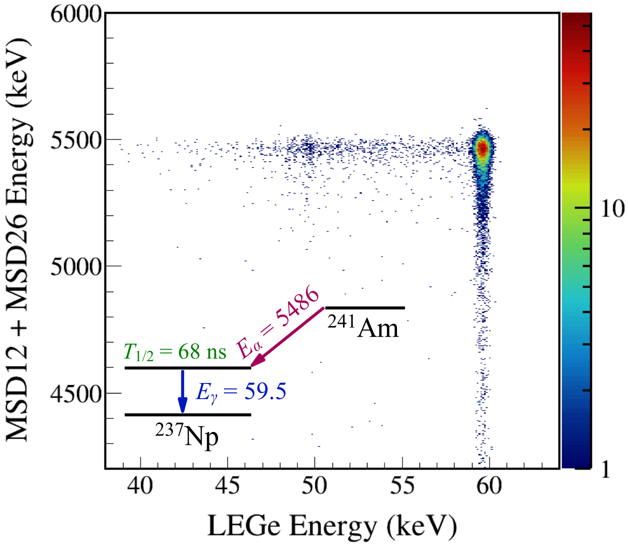

FIG. 14. Coincidence spectrum between the MSD detector telescope and LEGe obtained using the ^{241}Am source placed at the center of the chamber. A simplified ^{241}Am decay scheme shows the dominant α-γ sequence.

We placed the ^{152}Eu source at the center of the chamber. Figure 15 shows the XtRa1 γ spectra gated by the Sm K X rays measured by LEGe and gated by the electrons measured by MSD26, respectively. By applying the characteristic X-ray coincidence condition, both the room background γ rays and the ^{152}Gd γ rays are substantially suppressed. Conversely, the electron coincidence condition suppresses the room background and the ^{152}Sm γ rays. Having the ability to detect electrons and positrons would help clean up the in-beam spectrum, thereby facilitating the identification of γ ray origins.

E. Timing performance

The timing performance of electronics was first tested using a Canberra Model 1407P Pulse Pair Generator [84]. The dual pulses were separately fed into two Pixie-16 channels. The FWHM resolution of the time-difference distribution is estimated to be 0.46 ns. Then, the primary pulse was split and fed to each test input of preamplifiers, and the resulting FWHM timing resolutions are 37.4 ns (MSD12), 4.4 ns (MSD26), 1.2 ns (XtRa1), and 1.8 ns (XtRa2).

The timing performance of the detectors was studied using each of the ^{60}Co, ^{152}Eu, ^{241}Am sources placed at the center of the chamber. ^{60}Co provides γ-γ coincidences to test the two XtRa detectors, ^{152}Eu provides X-γ coincidences to test LEGe and XtRa, and ^{241}Am provides α-γ coincidences to test MSD and LEGe. Figure 16 shows the time difference distributions between each coincidence. Based on these measurements, an event-build window of a few hundred ns can be defined to capture all prompt coincidences and some chance continuum for background subtraction in offline analysis. Note that the asymmetric tail in both α-γ time difference distributions is attributed to the relatively long-lived 59.5-keV excited state of ^{237}Np.

Figure 17 shows the α-γ time difference distribution constructed by the start timestamps from 5486-keV α measured by the two MSDs and the stop timestamps from the 59.5-keV γ ray deexciting the 59.5-keV state in ^{237}Np measured by LEGe. By fitting the time spectra with a function

$$f(t; N, T_{1/2}, B) = \frac{N \ln(2)}{T_{1/2}} \exp\left[-\frac{t \ln(2)}{T_{1/2}}\right] + B \tag{5}$$

composed of the total number of decays (N), the exponential decay half-life ($T_{1/2}$), and a constant background (B), we obtained the half-life of the 59.5-keV excited state in ^{237}Np to be 68.1(6) ns (MSD12) and 67.9(5) ns (MSD26), respectively. Two factors may limit the time resolution that can be achieved with semiconductor detectors. Firstly, the charge collection process is inherently slow, typically taking several hundred nanoseconds. This timescale is much longer than the output from scintillators, making it hard to achieve the same level of timing performance. Secondly, the pulse rise shape from semiconductor detectors can vary significantly from event to event, resulting in a larger uncertainty in generating timestamps. Nevertheless, the results obtained from both Si detectors are consistent with recent precision measurements of 67.86(9) ns [86] and 67.60(25) ns [87], thereby providing validation for the PXCT electronics configurations.

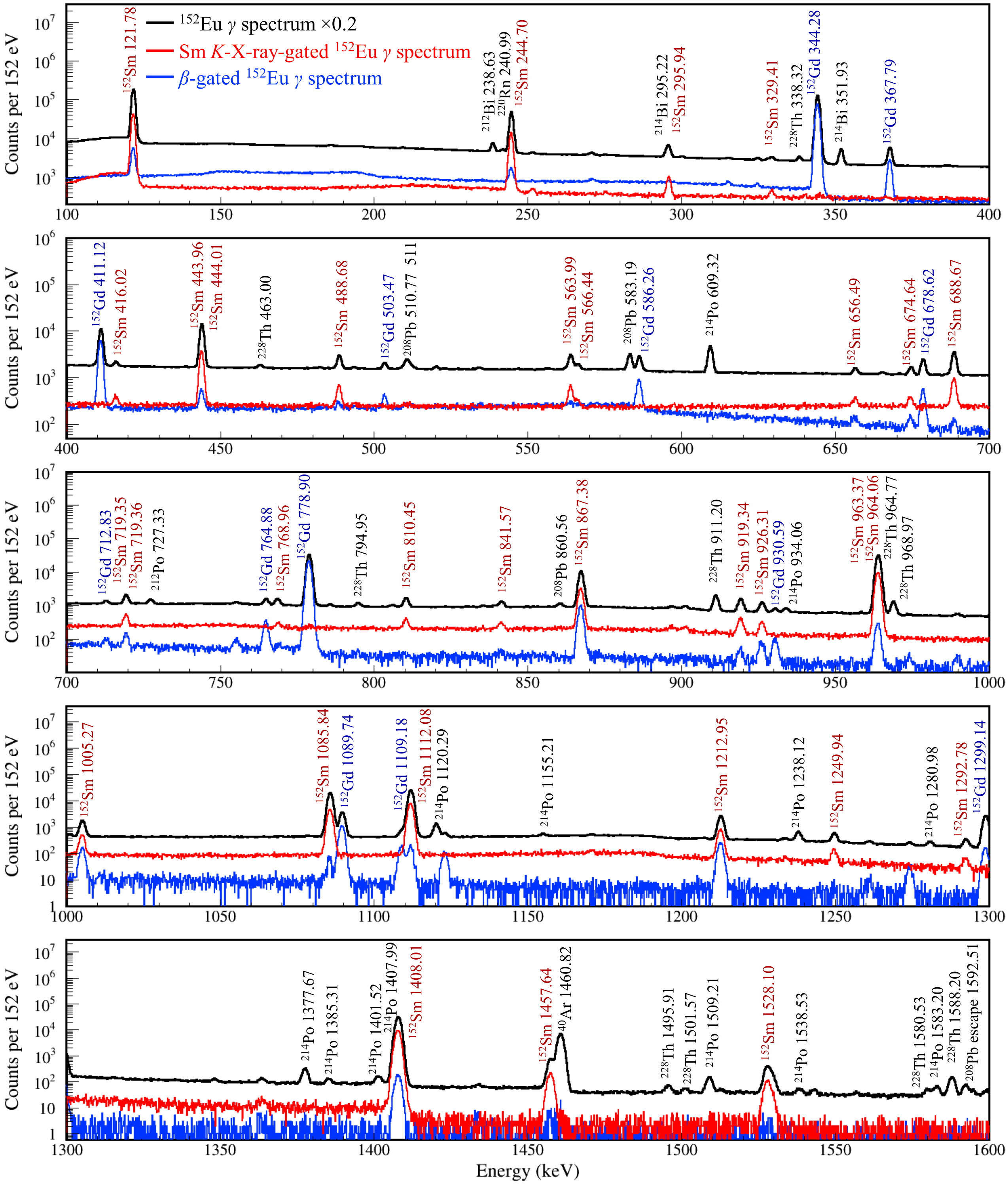

FIG. 15. Black represents the raw γ-ray spectrum measured by XtRa1 using the ^{152}Eu source placed at the center of the chamber. Red represents the XtRa1 γ-ray spectrum gated by the Sm K_α and K_β X rays measured by LEGe. Blue represents the XtRa1 γ-ray spectrum gated by the electrons measured by MSD26. The raw spectrum is scaled down by a factor of 5 for better comparison.

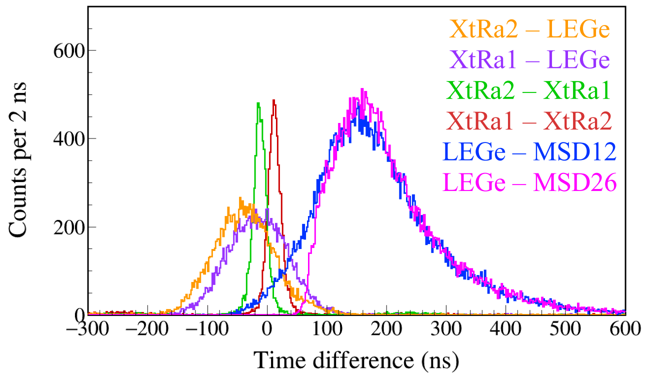

FIG. 16. Coincidence time spectra between each detector. From left to right: the six time peaks correspond to three decay sequences: the ^{152}Eu 40−46-keV and 1408-keV X-γ coincidences measured by XtRa-LEGe, the ^{60}Co 1173-keV and 1332-keV γ-γ coincidences measured by XtRa-XtRa, and the ^{241}Am 5486-keV and 59.5-keV α-γ coincidences measured by LEGe-MSD. In each decay sequence, the timestamp of the prior event is subtracted from the timestamp of the subsequent event.

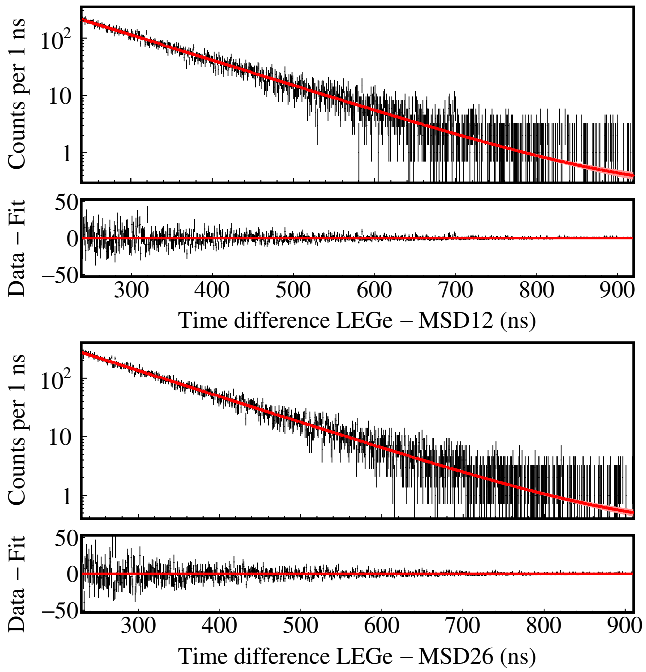

FIG. 17. Time differences between the 59.5-keV γ-ray signals in LEGe and the 5486-keV α signals in the MSD silicon detector telescope. From the fit, we obtain the $T_{1/2} = 68.1(6)$ ms, p-value $= 0.34$, and $\chi^2_\nu = 1.02$ by dividing the χ^2 value by the number of degrees of freedom, from LEGe-MSD12, and $T_{1/2} = 67.9(5)$ ms, p-value $= 0.88$, and $\chi^2_\nu = 0.94$ from LEGe-MSD26.

V. SUMMARY & OUTLOOK

We present the design, construction, simulation, and radioactive source testing of the PXCT detection system. Shell model calculations have revealed that only a handful of ^{60}Zn significantly contribute to the ^{59}Cu$(p,\gamma)^{60}$Zn thermonuclear reaction rate. The PXCT system is capable of detecting all types of charged particles and photons emitted in the EC/β^+ decay of ^{60}Ga, which will enable us to determine the branching ratios for proton, α, and γ rays and the lifetimes of discrete ^{60}Zn resonances for the first time. Alternatively, statistical analysis of the ^{60}Ga decay data can provide the nuclear level density and transmission coefficients needed for calculating astrophysical reaction rates using the statistical model. By acquiring a complete set of data on ^{60}Zn resonances using the PXCT system, we can gain valuable insights into the competition between the ^{59}Cu$(p,\gamma)^{60}$Zn and ^{59}Cu$(p,\alpha)^{56}$Ni reactions, enabling more accurate modeling of X-ray burst observables influenced by the NiCu cycle.

The PXCT system also holds the potential for constraining other key reaction rates in the *rp*-process. For instance, ^{64}Ge plays an analogous role in the ZnGa cycle (Fig. 1) to that of ^{60}Zn in the NiCu cycle [9]. Given the comparable Q_{EC}, half-lives, proton/α-separation energies, and X-ray energies, it is technically possible to extend this method to study the β decay of ^{64}As in the future.

VI. ACKNOWLEDGMENTS

We gratefully acknowledge the FRIB engineers for their technical assistance. We would like to thank Jun Chen for the helpful discussions. This work was supported by the U.S. National Science Foundation under Grants Nos. PHY-1913554, PHY-2110365, and PHY-2209429, and the U.S. Department of Energy, Office of Science, under Awards Nos. DE-SC0016052 and DE-SC0024587.

---

[1] J. José, *Stellar Explosions: Hydrodynamics and Nucleosynthesis* (CRC/Taylor and Francis: Boca Raton (FL), USA, 2016).

[2] H. Schatz and K. E. Rehm, Nucl. Phys. A **777**, 601 (2006).

[3] A. Parikh, J. José, G. Sala, and C. Iliadis, Prog. Part. Nucl. Phys. **69**, 225 (2013).

[4] L. van Wormer, J. Görres, C. Iliadis, M. Wiescher, and F.-K. Thielemann, Astrophys. J. **432**, 326 (1994).

[5] Richard H. Cyburt, A. Matthew Amthor, Ryan Ferguson, Zach Meisel, Karl Smith, Scott Warren, Alexander Heger, R. D. Hoffman, Thomas Rauscher, Alexander Sakharuk, Hendrik Schatz, F. K. Thielemann, Michael Wiescher, Astrophys. J. Suppl. Ser. **189**, 240 (2010).

[6] T. Rauscher and F. K. Thielemann, At. Data Nucl. Data Tables **75**, 1 (2000).

[7] T. Rauscher and F. K. Thielemann, At. Data Nucl. Data Tables **79**, 47 (2001).

[8] A. Parikh, J. José, F. Moreno, and C. Iliadis, Astrophys. J. Suppl. Ser. **178**, 110 (2008).

[9] R. H. Cyburt, A. M. Amthor, A. Heger, E. Johnson, L. Keek, Z. Meisel, H. Schatz, and K. Smith, Astrophys. J. **830**, 55 (2016).

[10] Zach Meisel, Grant Merz, and Sophia Medvid, Astrophys. J. **872**, 84 (2019).

[11] C. Fröhlich, G. Martínez-Pinedo, M. Liebendörfer, F.-K. Thielemann, E. Bravo, W. R. Hix, K. Langanke, and N. T. Zinner, Phys. Rev. Lett. **96**, 142502 (2006).

[12] A. Arcones, C. Fröhlich, and G. Martínez-Pinedo, Astrophys. J. **750**, 18 (2012).

[13] Kirby Hermansen, Sean M. Couch, Luke F. Roberts, Hendrik Schatz, MacKenzie L. Warren, Astrophys. J. **901**, 77 (2020).

[14] J. S. Randhawa, R. Kanungo, J. Refsgaard, P. Mohr, T. Ahn, M. Alcorta, C. Andreoiu, S. S. Bhattacharjee, B. Davids, G. Christian, A. A. Chen, R. Coleman, P. E. Garrett, G. F. Grinyer, E. Gyabeng Fuakye, G. Hackman, J. Hollett, R. Jain, K. Kapoor, R. Krücken, A. Laffoley, A. Lennarz, J. Liang, Z. Meisel, B. Nikhil, A. Psaltis, A. Radich, M. Rocchini, N. Saei, M. Saxena, M. Singh, C. Svensson, P. Subramaniam, A. Talebitaher, S. Upadhyayula, C. Waterfield, J. Williams, and M. Williams, Phys. Rev. C **104**, L042801 (2022).

[15] D. Soltesz, M. A. A. Mamun, A. V. Voinov, Z. Meisel, B. A. Brown, C. R. Brune, S. M. Grimes, H. Hadizadeh, M. Hornish, T. N. Massey, J. E. O'Donnell, and W. E. Ormand, Phys. Rev. C **103**, 015802 (2021).

[16] Chanhee Kim, Kyungyuk Chae, Soomi Cha, Kyujin Kwak, Gwangeon Seong, and Michael Smith, Astrophys. J. **929**, 96 (2022).

[17] Louis Wagner, unpublished.

[18] Connor O'Shea, unpublished.

[19] Gerard Owens-Fryar, unpublished.

[20] R. Mahajan, T. Wheeler, E. Pollacco, C. Wrede, A. Adams, H. Alvarez-Pol, A. Andalib, A. Anthony, Y. Ayyad, D. Bazin, T. Budner, M. Cortesi, J. Dopfer, M. Friedman, A. Jaros, D. Pérez-Loureiro, B. Mehl, R. De Oliveira, L. J. Sun, and J. Surbrook, Phys. Rev. C **109**, 06580x (2024).

[21] C. E. Rolfs and W. S. Rodney, *Cauldrons in the Cosmos* (University of Chicago, Chicago, 1988).

[22] T. Rauscher, Phys. Rev. C **81**, 045807 (2010).

[23] M. Wang, W. J. Huang, F. G. Kondev, G. Audi, S. Naimi, Chin. Phys. C **45**, 030003 (2021).

[24] S. E. A. Orrigo, B. Rubio, W. Gelletly, P. Aguilera, A. Algora, A. I. Morales, J. Agramunt, D. S. Ahn, P. Ascher, B. Blank, C. Borcea, A. Boso, R. B. Cakirli, J. Chiba, G. de Angelis, G. de France, F. Diel, P. Doornenbal, Y. Fujita, N. Fukuda, E. Ganioğlu, M. Gerbaux, J. Giovinazzo, S. Go, T. Goigoux, S. Grévy, V. Guadilla, N. Inabe, G. G. Kiss, T. Kubo, S. Kubono, T. Kurtukian-Nieto, D. Lubos, C. Magron, F. Molina, A. Montaner-

Pizá, D. Napoli, D. Nishimura, S. Nishimura, H. Oikawa, V. H. Phong, H. Sakurai, Y. Shimizu, C. Sidong, P.-A. Söderström, T. Sumikama, H. Suzuki, H. Takeda, Y. Takei, M. Tanaka, J. Wu, and S. Yagi, Phys. Rev. C **103**, 014324 (2021).

[25] S. F. Paul, J. Bergmann, J. D. Cardona, K. A. Dietrich, E. Dunling, Z. Hockenbery, C. Hornung, C. Izzo, A. Jacobs, A. Javaji, B. Kootte, Y. Lan, E. Leistenschneider, E. M. Lykiardopoulou, I. Mukul, T. Murböck, W. S. Porter, R. Silwal, M. B. Smith, J. Ringuette, T. Brunner, T. Dickel, I. Dillmann, G. Gwinner, M. MacCormick, M. P. Reiter, H. Schatz, N. A. Smirnova, J. Dilling, and A. A. Kwiatkowski, Phys. Rev. C **104**, 065803 (2021).

[26] Huo Junde, Huo Su, Yang Dong, Nucl. Data Sheets **112**, 1513 (2011).

[27] M. Shamsuzzoha Basunia, Nucl. Data Sheets **151**, 1 (2018).

[28] E. Browne and J. K. Tuli, Nucl. Data Sheets **114**, 1849 (2013).

[29] C. Mazzocchi, Z. Janas, J. Döring, M. Axiotis, L. Batist, R. Borcea, D. Cano-Ott, E. Caurier, G. de Angelis, E. Farnea, A. Faßbender, A. Gadea, H. Grawe, A. Jungclaus, M. Kapica, R. Kirchner, J. Kurcewicz, S.M. Lenzi, T. Martínez, I. Mukha, E. Nácher, D. R. Napoli, E. Roeckl, B. Rubio, R. Schwengner, J. L. Tain, and C. A. Ur, Eur. Phys. J. A **12**, 269 (2001).

[30] M. J. López Jiménez, B. Blank, M. Chartier, S. Czajkowski, P. Dessagne, G. de France, J. Giovinazzo, D. Karamanis, M. Lewitowicz, V. Maslov, C. Miehé, P. H. Regan, M. Stanoiu, and M. Wiescher, Phys. Rev. C **66**, 025803 (2002).

[31] L. Kucuk, S. E. A. Orrigo, A. Montaner-Pizá, B. Rubio, Y. Fujita, W. Gelletly, B. Blank, Y. Oktem, T. Adachi, A. Algora, P. Ascher, R. B. Cakirli, G. de France, H. Fujita, E. Ganioğlu, J. Giovinazzo, S. Grévy, F. M. Marqués, F. Molina, F. de Oliveira Santos, L. Perrot, R. Raabe, P. C. Srivastava, G. Susoy, A. Tamii, J. C Thomas, Eur. Phys. J. A **53**, 134 (2017).

[32] Gamma to Level Scheme Computation.

[33] R. Kamermans, H. W. Jongsma, J. van der Spek, and H. Verheul, Phys. Rev. C **10**, 620 (1974).

[34] Carl Svensson, Ph.D. Thesis, McMaster University, Ontario, Canada, 1998.

[35] M. Honma, T. Otsuka, B. A. Brown, and T. Mizusaki, Phys. Rev. C **69**, 034335 (2004).

[36] B. A. Brown and W. D. M. Rae, Nucl. Data Sheets **120**, 115 (2014).

[37] Radiation Report.

[38] J. C. Hardy, J. A. Macdonald, H. Schmeing, H. R. Andrews, J. S. Geiger, R. L. Graham, T. Faestermann, E. T. H. Clifford, and K. P. Jackson, Phys. Rev. Lett. **37**, 133 (1976).

[39] J. H. Scofield, *Atomic Inner-Shell Processes* (Academic Press: New York (NY), USA, 1975).

[40] W. Bambynek, B. Crasemann, R. W. Fink, H. U. Freund, H. Mark, C. D. Swift, R. E. Price, and P. Venugopala Rao, Rev. Mod. Phys. **44**, 716 (1972).

[41] J. Giovinazzo, Ph. Dessagne, and Ch. Miehé, Nucl. Phys. A **674**, 394 (2000).

[42] J. A. Macdonald, J. C. Hardy, H. Schmeing, T. Faestermann, H. R. Andrews, J. S. Geiger, R. L. Graham, and K. P. Jackson, Nucl. Phys. A **288**, 1 (1977).

[43] P. Asboe-Hansen, E. Hagberg, P. G. Hansen, J. C. Hardy, P. Hornshøj, B. Jonson, S. Mattsson, P. Tidemand-Petersson, Phys. Lett. B **77**, 363 (1978).

[44] P. Asboe-Hansen, E. Hagberg, P. G. Hansen, J. C. Hardy, B. Jonson, and S. Mattsson, Nucl. Phys. A **361**, 23 (1981).

[45] Z. Janas, L. Batist, R. Borcea, J. Döring, M. Gierlik, M. Karny, R. Kirchner, M. La Commara, S. Mandal, C. Mazzocchi, F. Moroz, S. Orlov, A. Płochocki, E. Roeckl, and J. Żylicz, Eur. Phys. J. A **24**, 205 (2005).

[46] Z. Janas, L. Batist, J. Döring, M. Gierlik, R. Kirchner, J. Kurcewicz, H. Mahmud, C. Mazzocchi, A. Płochocki, E. Roeckl, K. Schmidt, P. J. Woods, and J. Żylicz, Eur. Phys. J. A **23**, 401 (2005).

[47] C. Iliadis, *Nuclear Physics of Stars* (Wiley-VCH, Verlag, Wenheim, Germany, 2015).

[48] J. Wei, H. Ao, B. Arend, S. Beher, G. Bollen, N. Bultman, F. Casagrande, W. Chang, Y. Choi, S. Cogan, C. Compton, M. Cortesi, J. Curtin, K. Davidson, X. Du, K. Elliott, B. Ewert, A. Facco, A. Fila, K. Fukushima, V. Ganni, A. Ganshyn, J. Gao, T. Glasmacher, J. Guo, Y. Hao, W. Hartung, N. Hasan, M. Hausmann, K. Holland, H. C. Hseuh, M. Ikegami, D. Jager, S. Jones, N. Joseph, T. Kanemura, S.-H. Kim, P. Knudsen, B. Kortum, E. Kwan, T. Larter, R. E. Laxdal, M. Larmann, K. Laturkar, J. LeTourneau, Z.-Y. Li, S. Lidia, G. Machicoane, C. Magsig, P. Manwiller, F. Marti, T. Maruta, A. McCartney, E. Metzgar, S. Miller, Y. Momozaki, D. Morris, M. Mugerian, I. Nesterenko, C. Nguyen, W. O'Brien, K. Openlander, P. N. Ostroumov, M. Patil, A. S. Plastun, J. Popielarski, L. Popielarski, M. Portillo, J. Priller, X. Rao, M. Reaume, H. Ren, K. Saito, M. Smith, M. Steiner, A. Stolz, O. B. Tarasov, B. Tousignant, R. Walker, X. Wang, J. Wenstrom, G. West, K. Witgen, M. Wright, T. Xu, Y. Xu, Y. Yamazaki, T. Zhang, Q. Zhao, S. Zhao, K. Dixon, M. Wiseman, M. Kelly, K. Hosoyama, and S. Prestemon, Mod. Phys. Lett. A **37**, 2230006 (2022).

[49] M. Portillo, B.M. Sherrill, Y. Choi, M. Cortesi, K. Fukushima, M. Hausmann, E. Kwan, S. Lidia, P.N. Ostroumov, R. Ringle, M.K. Smith, M. Steiner, O.B. Tarasov, A.C.C. Villari, and T. Zhang, Nucl. Instrum. Methods Phys. Res. B **540**, 151 (2023).

[50] C.S. Sumithrarachchi, D.J. Morrissey, S. Schwarz, K. Lund, G. Bollen, R. Ringle, G. Savard, and A.C.C. Villari, Nucl. Instrum. Methods Phys. Res. B **463**, 305 (2020).

[51] K.R. Lund, G. Bollen, D. Lawton, D.J. Morrissey, J. Ottarson, R. Ringle, S. Schwarz, C.S. Sumithrarachchi, A.C.C. Villari, and J. Yurkon, Nucl. Instrum. Methods Phys. Res. B **463**, 378 (2020).

[52] A.C.C. Villari, G. Bollen, A. Henriques, A. Lapierre, S. Nash, R. Ringle, S. Schwarz, C.S. Sumithrarachchi, Nucl. Instrum. Methods Phys. Res. B **541**, 350 (2023).

[53] MIRCON MSD12 Circular Silicon Detector.

[54] MIRCON MSD26 Circular Silicon Detector.

[55] MIRION Low Energy Germanium Detector.

[56] MIRION Extended Range Coaxial Germanium Detector.

[57] MIRION Cryo-Pulse 5 PLUS Electrically Refrigerated Cryostat.

[58] D. Willems, R. Arts, B.V.-J. Douwen, MIRION Technical Paper (2015).

[59] MIRION Intelligent Preamplifier.

[60] ORTEC 660 Dual 5-kV Bias Supply.

[61] Mesytec MPR-1 Charge Integrating Preamplifier.

[62] Mesytec MHV-4 High Voltage Supply.

[63] Mesytec MNV-4 NIM Power Supply.

[64] XIA Pixie-16 Digitizer.

[65] K. Starosta, C. Vaman, D. Miller, P. Voss, D. Bazin, T. Glasmacher, H. Crawford, P. Mantica, H. Tan, W. Hennig, M. Walby, A. Fallu-Labruyere, J. Harris, D. Breus, P. Grudberg, W.K. Warburton, Nucl. Instrum. Methods Phys. Res. A **610**, 700 (2009).

[66] C.J. Prokop, S.N. Liddick, B.L. Abromeit, A.T. Chemey, N.R. Larson, S. Suchyta, J.R. Tompkins, Nucl. Instrum. Methods Phys. Res. A **741**, 163 (2014).

[67] XIA Pixie-16 Digitizer User Manual.

[68] H.Y. Wu, Z.H. Li, H. Tan, H. Hua, J. Li, W. Hennig, W.K. Warburton, D.W. Luo, X. Wang, X.Q. Li, S.Q. Zhang, C. Xu, Z.Q. Chen, C.G. Wu, Y. Jin, J. Lin, D.X. Jiang, Y.L. Ye, Nucl. Instrum. Methods Phys. Res. A **975**, 164200 (2020).

[69] D. Weisshaar, D. Bazin, P.C. Bender, C.M. Campbell, F. Recchia, V. Bader, T. Baugher, J. Belarge, M.P. Carpenter, H.L. Crawford, M. Cromaz, B. Elman, P. Fallon, A. Forney, A. Gade, J. Harker, N. Kobayashi, C. Langer, T. Lauritsen, I.Y. Lee, A. Lemasson, B. Longfellow, E. Lunderberg, A.O. Macchiavelli, K. Miki, S. Momiyama, S. Noji, D.C. Radford, M. Scott, J. Sethi, S.R. Stroberg, C. Sullivan, R. Titus, A. Wiens, S. Williams, K. Wimmer, S. Zhu, Nucl. Instrum. Methods Phys. Res. A **847**, 187 (2017).

[70] BNC Model DB-2 NIM Random Pulse Generator.

[71] L. J. Sun, M. Friedman, T. Budner, D. Pérez-Loureiro, E. Pollacco, C. Wrede, B. A. Brown, M. Cortesi, C. Fry, B. E. Glassman, J. Heideman, M. Janasik, A. Kruskie, A. Magilligan, M. Roosa, J. Stomps, J. Surbrook, and P. Tiwari, Phys. Rev. C **103**, 014322 (2021).

[72] Matt Newville, easyXAFS, Matteo Levantino, Christian Schlepuetz, Damian Günzing, Max Rakitin, Sang-Woo Kim, and kalvdans, xraypy/XrayDB: (4.5.1). Zenodo (2023).

[73] M.-M. Bé, V. Chisté, C. Dulieu, X. Mougeot, E. Browne, V. Chechev, N. Kuzmenko, F. Kondev, A. Luca, M. Galán, A.L. Nichols, A. Arinc, and X. Huang, Table of Radionuclides, Bureau International des Poids et Mesures (2004).

[74] Devinder Mehta, M.L. Garg, Jasbir Singh, Nirmal Singh, T.S. Cheema, P.N. Trehan, Nucl. Instrum. Methods Phys. Res. A **245**, 447 (1986).

[75] M. Basunia, Nucl. Data Sheets **107**, 2323 (2006).

[76] M. J. Martin, Nucl. Data Sheets **114**, 1497 (2013).

[77] B. E. Glassman, D. Pérez-Loureiro, C. Wrede, J. Allen, D. W. Bardayan, M. B. Bennett, K. A. Chipps, M. Febbraro, M. Friedman, C. Fry, M. R. Hall, O. Hall, S. N. Liddick, P. O'Malley, W. -J. Ong, S. D. Pain, S. B. Schwartz, P. Shidling, H. Sims, L. J. Sun, P. Thompson, and H. Zhang, Phys. Rev. C **99**, 065801 (2019).

[78] S. Agostinelli, J. Allison, K. Amako, J. Apostolakis, H. Araujo, P. Arce, M. Asai, D. Axen, S. Banerjee, G. Barrand, F. Behner, L. Bellagamba, J. Boudreau, L. Broglia, A. Brunengo, H. Burkhardt, S. Chauvie, J. Chuma, R. Chytracek, G. Cooperman, G. Cosmo, P. Degtyarenko, A. Dell'Acqua, G. Depaola, D. Dietrich, R. Enami, A. Feliciello, C. Ferguson, H. Fesefeldt, G. Folger, F. Foppiano, A. Forti, S. Garelli, S. Giani, R. Giannitrapani, D. Gibin, J. J. Gómez Cadenas, I. González, G. Gracia Abril, G. Greeniaus, W. Greiner, V. Grichine, A. Grossheim, S. Guatelli, P. Gumplinger, R. Hamatsu, K. Hashimoto, H. Hasui, A. Heikkinen, A. Howard, V. Ivanchenko, A. Johnson, F. W. Jones, J. Kallenbach, N. Kanaya, M. Kawabata, Y. Kawabata, M. Kawaguti, S. Kelner, P. Kent, A. Kimura, T. Kodama, R. Kokoulin, M. Kossov, H. Kurashige, E. Lamanna, T. Lampén, V. Lara, V. Lefebure, F. Lei, M. Liendl, W. Lockman, F. Longo, S. Magni, M. Maire, E. Medernach, K. Minamimoto, P. Mora de Freitas, Y. Morita, K. Murakami, M. Nagamatu, R. Nartallo, P. Nieminen, T. Nishimura, K. Ohtsubo, M. Okamura, S. O'Neale, Y. Oohata, K. Paech, J. Perl, A. Pfeiffer, M. G. Pia, F. Ranjard, A. Rybin, S. Sadilov, E. Di Salvo, G. Santin, T. Sasaki, N. Savvas, Y. Sawada, S. Scherer, S. Sei, V. Sirotenko, D. Smith, N. Starkov, H. Stoecker, J. Sulkimo, M. Takahata, S. Tanaka, E. Tcherniaev, E. Safai Tehrani, M. Tropeano, P. Truscott, H. Uno, L. Urban, P. Urban, M. Verderi, A. Walkden, W. Wander, H. Weber, J. P. Wellisch, T. Wenaus, D. C. Williams, D. Wright, T. Yamada, H. Yoshida, and D. Zschiesche, Nucl. Instrum. Methods Phys. Res. A **506**, 250 (2003).

[79] J. Allison, K. Amako, J. Apostolakis, P. Arce, M. Asai, T. Aso, E. Bagli, A. Bagulya, S. Banerjee, G. Barrand, B.R. Beck, A.G. Bogdanov, D. Brandt, J.M.C. Brown, H. Burkhardt, Ph. Canal, D. Cano-Ott, S. Chauvie, K. Cho, G.A.P. Cirrone, G. Cooperman, M.A. Cortés-Giraldo, G. Cosmo, G. Cuttone, G. Depaola, L. Desorgher, X. Dong, A. Dotti, V.D. Elvira, G. Folger, Z. Francis, A. Galoyan, L. Garnier, M. Gayer, K.L. Genser, V.M. Grichine, S. Guatelli, P. Guèye, P. Gumplinger, A.S. Howard, I. Hřivnáčová, S. Hwang, S. Incerti, A. Ivanchenko, V.N. Ivanchenko, F.W. Jones, S.Y. Jun, P. Kaitaniemi, N. Karakatsanis, M. Karamitros, M. Kelsey, A. Kimura, T. Koi, H. Kurashige, A. Lechner, S.B. Lee, F. Longo, M. Maire, D. Mancusi, A. Mantero, E. Mendoza, B. Morgan, K. Murakami, T. Nikitina, L. Pandola, P. Paprocki, J. Perl, I. Petrović, M.G. Pia, W. Pokorski, J.M. Quesada, M. Raine, M.A. Reis, A. Ribon, A. Ristić Fira, F. Romano, G. Russo, G. Santin, T. Sasaki, D. Sawkey, J.I. Shin, I.I. Strakovsky, A. Taborda, S. Tanaka, B. Tomé, T. Toshito, H.N. Tran, P.R. Truscott, L. Urban, V. Uzhinsky, J.M. Verbeke, M. Verderi, B.L. Wendt, H. Wenzel, D.H. Wright, D.M. Wright, T. Yamashita, J. Yarba, H. Yoshida, Nucl. Instrum. Methods Phys. Res. A **835**, 186 (2016).

[80] Erik Jensen, Ph.D. Thesis, Aarhus University, Aarhus, Denmark, 2024.

[81] FRIB Decay Station White Paper.

[82] Y.A. Akovali, Nucl. Data Sheets **84**, 1 (1998).

[83] M.-M. Bé, V. Chisté, C. Dulieu, X. Mougeot, E. Browne, V. Chechev, N. Kuzmenko, F. Kondev, A. Luca, M. Galán, A.L. Nichols, A. Arinc, and X. Huang, Table of Radionuclides, Bureau International des Poids et Mesures (2010).

[84] Canberra Model 1407P Pulse Pair Generator.

[85] D. Foreman-Mackey, D. W. Hogg, D. Lang, and J. Goodman, Publ. Astron. Soc. Pac. **125**, 306 (2013).

[86] Marcell P. Takács, Karsten Kossert, Appl. Radiat. Isot. **176**, 109858 (2021).

[87] Chavdar Dutsov, Benoît Sabot, Philippe Cassette, Krasimir Mitev, Appl. Radiat. Isot. **176**, 109845 (2021).